Chaotic dynamics in small inert gas clusters: The influence of potential energy saddles

Robert J. Hinde[a] and R. Stephen Berry

Department of Chemistry and the James Franck Institute, The University of Chicago, 5735 South Ellis Avenue, Chicago, Illinois 60637

We have investigated the effect of potential energy saddles on the evolution of chaos in small (three- to seven-atom) inert gas clusters by comparing the local Kolmogorov entropy (K entropy) accumulated near a saddle with that accumulated in a potential well. We find that saddles which are relatively flat along the isomerization coordinate are most effective at reducing the local K entropy in the saddle region, indicating that these saddles tend to regularize the dynamics close to the saddle point. In three- and four-atom clusters, we also find that flat saddles decouple some or all of the cluster's vibrational modes from one another; this leads to approximately quasiperiodic behavior in some degrees of freedom near the saddle regions of these clusters.

I. INTRODUCTION

In the last three decades, chaotic dynamics in chemically relevant Hamiltonian systems has become an increasingly active field of research. This is in part due to our recognition that the vast majority of nonlinear Hamiltonian systems, including those systems of coupled anharmonic oscillators typically used to model molecular vibrations, exhibit some degree of chaos. Interest in the chaotic dynamics of molecules also stems from the fact that chaotic systems are both ergodic and mixing;[1] hence nonequilibrium ensembles of chaotic molecules relax to give statistical equilibrium expectation values of dynamical observables.[2]

Many of the earliest investigations of chaos in molecular systems were concerned simply with determining "how chaotic" a particular model Hamiltonian was at a given energy. The numerical diagnostics available for answering such a question are the Liapunov exponents,[3] which measure the asymptotic long-time rate of divergence (or convergence) of nearby trajectories in phase space, and the Kolmogorov entropy[4] (K entropy), which is the sum of a system's positive Liapunov exponents.[5] The K entropy measures the long-time rate of stretching of small volumes of phase space, or, equivalently, the rate at which we lose information about the initial state of our system.[6] A system with at least one positive Liapunov exponent is chaotic, and the magnitude of a system's K entropy tells us "how chaotic" the system is. (The situation is complicated slightly by the fact that chaotic and regular components of phase space can intermingle over a range of energies, and so to fully answer the question of how chaotic a dynamical system is, we must also measure the fraction of phase space occupied by chaotic trajectories.[7,8])

Because the algorithms used to calculate Liapunov exponents are computationally intensive, early studies of chaotic Hamiltonian dynamics were often limited to model

systems with only a few degrees of freedom; the canonical system introduced by Hénon and Heiles,[7] for example, has only two degrees of freedom. In the last decade, however, it has become feasible to compute the entire spectrum of Liapunov exponents for realistic molecular systems with as many as a few dozen degrees of freedom, and for very long times. These investigations have shown that the Liapunov spectrum and K entropy of a system may contain a variety of interesting information in addition to answering the question of whether a system is chaotic. For example, Livi, Vulpiani, and co-workers[9–12] have recently attempted to uncover the significance of the shape of the Liapunov spectrum and its limiting form as the number of degrees of freedom becomes very large. Posch and co-workers[13–15] have calculated the Liapunov exponents of dense fluid systems with periodic boundary conditions; they observe interesting changes in the shape of the Liapunov spectrum with density and with the number of spatial dimensions. (They have also computed the rotation numbers[15,16] associated with the Liapunov exponents; it is not yet clear what dynamical significance these numbers have.) Cleary[17] has interpreted steplike fluctuations in the Liapunov exponents on a very long time scale (10^6–10^8 time steps) as signifying the exploration of dynamically different regions of phase space.

Along similar lines, Amitrano and Berry[18] have shown that the time evolution of the sample distribution of *local* Liapunov exponents can be a useful tool to distinguish dynamically different regions of phase space in realistic molecular systems, and can provide insight into the time scale on which ergodic behavior among these regions is established. The local Liapunov exponents are finite-time analogs of the Liapunov exponents, and measure the rate of divergence or convergence of nearby phase space trajectories over short periods of time. The local K entropy, which is the sum of the positive local Liapunov exponents, measures the short-time stretching of phase space volumes along a trajectory. Abarbanel, Brown, and Kennel[19] have also computed the local Liapunov exponents of some model systems, all of which are non-Hamiltonian. They

[a]Present address: Department of Chemistry, Baker Laboratory, Cornell University, Ithaca, NY 14853-1301.

observe different types of power-law convergence of the local Liapunov exponents to the asymptotic (global) Liapunov exponents. (In connection with this point, they emphasize that the convergence of local Liapunov exponents to the asymptotic Liapunov exponents is only incompletely understood.) Abarbanel, Brown, and Kennel also show that the shape of the local Liapunov exponent distributions can help quantify the degree of short-time or "regional" predictability in different portions of phase space.

We report here the results of a study of the local K entropy of homogeneous clusters with three to seven atoms bound by pairwise Lennard-Jones or Morse pair potentials; in particular, we are interested in comparing the local K entropy for trajectory segments near potential minima with that for trajectory segments near saddles on the potential surface. Our interest in the behavior of clusters in the vicinity of potential energy saddles stems from two considerations. First, saddles are ubiquitous features of the potential surfaces of loosely bound systems such as clusters and van der Waals complexes; a thorough analysis of the behavior of these systems in the saddle regions is important to our understanding of dynamical phenomena such as unimolecular isomerization[20] and the transition from solid-like to liquidlike behavior in clusters.[21,22] Second, recent work of ours[23] has shown that in Ar_3, the curvatures of the potential surface near the saddle (associated with a collinear configuration of the three atoms) play a crucial role in determining how the cluster's K entropy varies with its total energy. This previous work showed that in Ar_3, the saddle region sometimes acted to collimate the flow of neighboring trajectories, thereby reducing the degree of chaos in the cluster. However, we found no evidence of similar behavior in Ar_7. Our aim in the present study is to probe more deeply into the mechanisms by which saddle regions may control the evolution of chaos in small clusters, and in particular to determine to what degree the properties of the saddle region in the Ar_3 cluster are generic and representative of larger clusters.

Recent work by Pettini[24] provides another motivation for studying the evolution of chaos in small systems in terms of the shape of the potential energy surface. In this work, Pettini used tools of Riemannian differential geometry to search for a relationship between the curvature of configuration space manifolds and the strong-stochasticity threshold in Fermi–Pasta–Ulam and ϕ^4 chains. He found that in these systems, the onset of chaotic behavior was closely linked to a major change in the topology of the underlying configuration space manifold which could be measured by the manifold's scalar or Ricci curvature; furthermore, he suggested that an analysis of chaotic dynamics based on topological considerations may ultimately prove more useful than the usual homoclinic intersection picture, especially in systems with many degrees of freedom.

The paper is organized as follows. In Sec. II we describe the method by which we isolate segments of phase space trajectories near potential minima or potential saddles; this will permit us to introduce a specialized, but natural, notation for presenting our results. In this section,
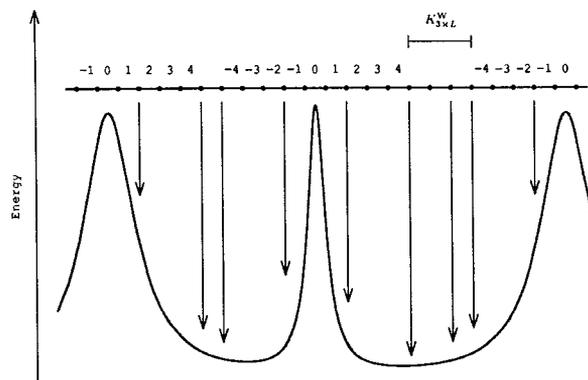

FIG. 1. Schematic representation of a molecular dynamics trajectory on a multidimensional potential energy surface. The horizontal line with dots represents the constant energy trajectory; each dot signifies a steepest-descent quench. Some quenches have been represented by arrows; for the sake of clarity, only a few quenches are shown explicitly. The numeric labels on the MD trajectory are described in the text.

we also describe the way in which we calculate the local K entropy for trajectory segments and make some general remarks on the local Liapunov exponents and local K entropy. In Sec. III we present our results, organized both by cluster size and by the form of the pairwise binding potential. We then discuss these results in terms of the underlying features of the potential energy surfaces of these clusters. Section IV discusses a method by which results obtained for different clusters can be placed on an "equal footing" for comparision. Finally, in Sec. V we summarize the main conclusions of the paper and indicate the chemical relevance of our findings.

II. COMPUTATIONAL METHOD

We begin our calculations by generating phase space trajectories for a cluster using conventional isoergic molecular dynamics (MD) techniques. We use the velocity Verlet method[25,26] for propagating our trajectories forward in time; unless otherwise specified, we use an integration time step of $\Delta t = 10^{-14}$ s.

To isolate segments of a trajectory near potential energy saddles, we perform steepest descent quenches on the cluster at periodic intervals of L time steps (Fig. 1). We typically set $L = 500$, although for six- and seven-atom clusters we quench more frequently. When the end points of the steepest-descent quenches abruptly switch from one minimum to another (different atomic permutations of the same geometric configuration are considered to be distinct minima), we know that the MD trajectory has crossed a saddle which separates these two minima.

Once we have isolated an isomerization, we assign integer labels to the L-step segments of the MD trajectory near the saddle point, as shown in Fig. 1. The segment in which the isomerization occurs is labeled "0"; segments at progressively earlier and later times are labeled with negative and positive integers, respectively. By piecing together several consecutive L-step segments, we can generate portions of our MD trajectory of any desired length,

provided the total length is a multiple of L time steps, and whose (temporal) proximity to the saddle point is known to within the quench interval of L steps. These pieced-together segments are the fundamental dynamical entities whose properties we shall consider in this paper.

We restrict our attention to sections of the MD trajectory assembled from an odd number of consecutive L-step segments so that we may define a unique central L-step segment for each portion. The label of this central segment, along with the length of the entire assembled section, together locate any section of the MD trajectory with respect to a nearby saddle point. We now introduce a special notation which uses these two identifying features.

Suppose we calculate some quantity Q for the set $\{n-k,...,n+k\}$ of $2k+1$ L-step segments centered on the segment labeled n; we represent the result of this calculation as $Q^n_{(2k+1)\times L}$, where the subscripts specify the total length of the trajectory segment and the superscript indicates how close this segment is to the saddle point. As a specific example, we will later be interested in comparing the local K entropy K of the 1500-step segment which includes the saddle crossing with the local K entropy of the 1500-step segments which immediately precede and follow this "crossing segment." If the quench interval L in Fig. 1 is 500 time steps, then the set $\{-1,0,1\}$ comprises the 1500-step segment centered on the saddle crossing, and the local K entropy for this segment is just $K^0_{3\times500}$. For the preceding and following 1500-step segments, which are defined by the sets $\{-4,-3,-2\}$ and $\{2,3,4\}$, the local K entropy is given by $K^{-3}_{3\times500}$ and $K^3_{3\times500}$, respectively.

We also examine segments of the MD trajectory which are temporally removed from any isomerizations, and which therefore represent motion in a single potential well. We do this by locating sequential portions of the trajectory lying in the same potential well or catchment basin. We will denote quantities calculated for these trajectory segments with a superscript W (for well); as an example, the local K entropy for a set of three consecutive 500-step segments in a single potential minimum is given by $K^W_{3\times500}$. For saddles which connect two nondegenerate minima, we use the superscripts UW and LW to distinguish between the upper and lower wells.

We have focused our attention on these short trajectory segments in order to determine to what extent small clusters exhibit different dynamical behavior on different regions of the potential surface. Hence it is essential that our system for classifying the trajectory segments be unambiguous. For example, at high energies where the time between isomerizations is relatively short, the 1500-step segment following a saddle crossing (i.e., the segment defining $K^3_{3\times500}$) may partially overlap the 1500 steps preceding the next saddle crossing ($K^{-3}_{3\times500}$) or the 1500-step segment in the potential well between these saddles ($K^W_{3\times500}$). To avoid ambiguities of this nature, we select only those portions of our MD trajectories where the residence time in two neighboring potential wells is long enough to ensure that there is no overlap between different types of trajectory segments.

Now we define the dynamical quantities which we cal-

culate for MD trajectory segments. We distinguish between quantities which are defined only over an extended trajectory segment, such as the local Liapunov exponents and local K entropy, and quantities defined for an instantaneous configuration of our system, and which we can therefore *average* over a segment of the trajectory. We use angle brackets to denote this averaging process; for example, the mean kinetic energy of a cluster over the 1500-step segment centered on the saddle crossing would be $\langle E_{kin}\rangle^0_{3\times500}$.

The primary quantities of interest in this work are the local Liapunov exponents and local K entropy of our system. The local Liapunov exponents for an L-step portion of a phase space trajectory are calculated by diagonalizing the product of L Jacobian matrices along the trajectory.[3] If $\mathbf{x}(t)=(q_{1x},q_{1y},...,q_{Nz},p_{1x},p_{1y},...,p_{Nz})^T$ specifies a point on the phase space trajectory of an N-atom cluster, and $\mathbf{J}(\mathbf{x})$ is the phase space Jacobian matrix at $\mathbf{x}$, then the local Liapunov exponents and local K entropy are obtained as follows. First, we construct the matrix $\mathbf{K}=\Pi^{L-1}_{n=0}\mathbf{J}(\mathbf{x}(t+n\Delta t))$ and compute its eigenvalues $\{k_j\}$. The local Liapunov exponents for this L-step trajectory segment are given by $\lambda_j=(\log_2|k_j|)/L\Delta t$. The local K entropy K is just the sum of the positive local Liapunov exponents. We use an approximate formula for $\mathbf{J}$ which is second order in the time step Δt; the details of this formula are given in Ref. 23. Note that different degrees of "locality" can be obtained by choosing different values of L.[18,27]

Meyer[28] has proven a number of important theorems concerning the Liapunov exponents of Hamiltonian systems, many of which are valid for local Liapunov exponents as well. Of particular importance for the current work are the facts that (1) the Liapunov exponents come in matching positive/negative pairs, in accordance with Liouville's theorem, and (2) there must be at least $2C$ zero Liapunov exponents if there are C independent constants of motion. In the present study, our phase space trajectories preserve seven independent constants of motion, namely three Cartesian components of both linear and angular momentum, and the total energy. Hence we expect to find 14 zero local Liapunov exponents for each trajectory segment. In reality, a short trajectory segment often exhibits only 10 or 12 zero local Liapunov exponents; this may be related to the convergence properties of the local Liapunov exponents. For an N-atom cluster, the local K entropy K we report here is the sum of the largest $3N-7$ local Liapunov exponents for a given trajectory segment; this formula excludes those local Liapunov exponents which vanish in the asymptotic limit. (The results we present here, however, hold as well for the *uncorrected* local K entropy computed from the sum of *all* positive local Liapunov exponents.) The local Liapunov exponents we calculated always appear in matching positive/negative pairs as expected.

We will later be interested in comparing the trends in the local K entropy of our clusters with those exhibited by the time-averaged kinetic energy of a cluster. All of our MD simulations are conducted under conditions of zero linear and angular momentum, so that the kinetic energy

of a cluster is completely vibrational. Hence we convert the kinetic energy of our clusters into an internal vibrational temperature, both to introduce more intuitive units and to facilitate comparisons between clusters of different sizes. The vibrational temperature of an N-atom cluster is given by $T = 2E_{kin}/(3N-6)k_B$, where k_B is Boltzmann's constant in appropriate units.

It is useful to analyze the trends in the local K entropy of our clusters on the basis of the degree of coupling among a cluster's vibrational modes. To quantify this coupling, we use an adaptation of the mathematical framework developed by Miller, Handy, and Adams[29] in their studies of reaction path Hamiltonians. At each time step along a given MD trajectory segment, we diagonalize the Hessian matrix of our N-atom cluster, obtaining $3N-6$ unit eigenvectors $\{\hat{u}_j\}$ which are just the cluster's local normal modes. (We use standard projection matrix techniques[30] to eliminate infinitesimal rotations and translations.) We also obtain $3N-6$ corresponding eigenvalues $\{\omega_j^2\}$, which are the squares of the normal mode vibrational frequencies. We order the modes in order of increasing eigenvalues, so that $\omega_1^2 < \omega_2^2 < \cdots < \omega_{3N-6}^2$.

Following Miller, Handy, and Adams, we define the coupling between two different modes j and k as $b_{jk} = \hat{u}_k \cdot d\hat{u}_j/dt$. This coupling element essentially measures how much mode $\hat{u}_j$ rotates into mode $\hat{u}_k$ as the cluster moves along the MD trajectory. In a region of the potential surface where some mode $\hat{u}_k$ becomes approximately decoupled from the other modes $\{\hat{u}_j\}$, $\hat{u}_k$ should remain roughly constant. Hence b_{jk} should be small in this area of the potential surface. [Note that the indices in b_{jk} refer to the vibrational modes of the cluster at a given instant, sorted according to the corresponding Hessian eigenvalues. For example, $b_{12}(t)$ is the instantaneous coupling at time t between the modes with the two smallest Hessian eigenvalues.]

Page and McIver[30] give an analytical formula for b_{jk}:

$$b_{jk} = \frac{\hat{u}_k^T \cdot dH/dt \cdot \hat{u}_j}{\omega_j^2 - \omega_k^2}, \tag{1}$$

where H is the cluster's instantaneous Hessian matrix. However, analytic evaluation of dH/dt requires lengthy computations of the third derivatives of the potential surface. Instead, we approximate $d\hat{u}_j/dt$ by the expression $[\hat{u}_j(t+\Delta t) - \hat{u}_j(t)]/\Delta t$. Comparison of these two approaches for a three-atom cluster showed that this approximate method is sufficiently accurate for our purposes when $\Delta t = 10^{-14}$ s. Finally, we reduce the matrix $\{b_{jk}\}$ to a manageable amount of data for analysis by focusing on the root mean square average of the coupling elements:

$$C = \left(\frac{\Sigma_{j \neq k} b_{jk}^2}{(3N-6)(3N-7)} \right)^{1/2},$$

which measures in a crude sense the *total* coupling among a cluster's vibrational modes.

We would ultimately like to relate the trends in the local K entropy of a cluster to some simple properties of the cluster's underlying potential surface. Wales and

Berry[27] made substantial progress in this direction by considering the local K entropy accumulated by a cluster or molecule during a single MD time step. In the limit as the step size $\Delta t \to 0$, they obtained a simple formula for the one-step local K entropy in terms of the imaginary local vibrational frequencies $\{\omega_j\}$ of the system:

$$K_\omega = \sum_{\omega_j^2 < 0} |\omega_j^2|^{1/2}/\ln 2.$$

(Wales and Berry originally called this quantity K^1; here, we emphasize its relationship to the cluster's vibrational frequencies by using the symbol K_ω.) Like the temperature or mean vibrational coupling C, this quantity is defined for an instantaneous configuration of our cluster. The relationship between a molecule's instantaneous imaginary frequencies and its local K entropy is easy to understand if we recognize that negatively curved portions of the potential surface induce divergence in bundles of MD trajectories traveling perpendicular to the direction of negative curvature.[31] Note that because ω_j is a frequency, K_ω (like the local K entropy) has units of bits per unit time. We emphasize that K_ω can be interpreted either *dynamically* as an approximate instantaneous local K entropy or *structurally* as the magnitude of negative curvature at a point in configuration space.

We end this section with a few comments on the limitations of our method for locating saddle crossings. We have adopted the present algorithm for locating saddles because for inert gas clusters with five or more atoms, there is no simple geometric coordinate, such as a bond or torsion angle, which suffices to define the reaction coordinate connecting two neighboring potential minima. Hence periodic quenching is a convenient method for locating a cluster on its potential surface. One drawback of this approach is that quenches are computationally expensive. In addition, if our quench interval is too large, we may miss instances in which a saddle is crossed in one direction and rapidly recrossed in the other direction, and may incorrectly identify such a segment of the trajectory as one which has remained in a single minimum for a long time. We can overcome this difficulty by quenching more frequently; however, this dramatically increases the CPU time required for our calculations.

It is also possible that a trajectory segment which actually does remain within a given minimum for a long time may stray close to a saddle point without our knowledge, because we do not directly monitor the reaction coordinate for the isomerization process. For the same reason, in cases where two or more nondegenerate saddles connect the same two minima, we will not be able to determine which saddle was involved in the isomerization.

Finally, our method for locating saddle crossings is effectively applicable over only a limited range of energies. This is not a result of our use of quenches; it is simply a complication introduced by the dynamics of our clusters. If the energy of our MD trajectory is too low, isomerizations will be relatively infrequent events and we will need to generate very long trajectories to assemble a statistically

significant pool of data. On the other hand, if the trajectory energy is too high, saddle crossings occur so frequently that they begin to overlap, so that we cannot classify our trajectory segments unambiguously. This limitation is only serious with clusters of seven or more atoms; because of the large number of degrees of freedom in these clusters and the large number of minima and saddles on their potential surfaces, we must generate MD trajectories with fairly high energies if we are to observe any isomerizations at all. It seems to us that the seven-atom cluster may be close to the largest for which the present algorithm is practical.

III. RESULTS AND INTERPRETATION

In this section, we present our results for three- through seven-atom Lennard-Jones clusters and for three- and five-atom Morse clusters. We present and discuss our results for each cluster in a separate subsection, deferring until Sec. V a discussion of the entire body of results. For brevity, we will henceforth use the symbols LJ_N and M_N as abbreviations for N-atom Lennard-Jones and Morse clusters, respectively. In all of the clusters we describe here, we have chosen the atomic mass to be $m = 39.948$ amu and the well depth of the interatomic pair potential to be $\epsilon = 121$ K. For the Lennard-Jones potential, we set $\sigma = 3.405$ Å, and for the Morse potential, we set the equilibrium bond length $r_0 = 3.822$ Å. These parameters correspond to those generally used in simulations of argon clusters. We vary ρ, the dimensionless range parameter for the Morse potential, to generate different potential surfaces for Morse clusters of a given size.[32] Small values of ρ correspond to long-range Morse pair potentials, and a Morse potential with $\rho = 6$ is similar to a Lennard-Jones pair potential. (The actual pair potential for Ar_2 is closely approximated by $\rho = 5.72$.[33]) All of our calculations have been performed on an IBM RS/6000 workstation.

A. LJ_3 clusters

Here we discuss our results for a nonrotating three-atom Lennard-Jones cluster, which has a particularly simple potential energy surface. To help interpret our results, we review briefly the stationary points on this surface. The global minimum is located at energy $E = -3.00$ ϵ, where the cluster assumes the shape of an equilateral triangle. There are three equivalent but permutationally distinct saddle points at $E = -2.031$ ϵ which correspond to a collinear configuration of the atoms.

In Fig. 2 we show the probability distributions for several dynamical quantities calculated on different portions of the LJ_3 potential surface. We describe this figure in some detail here because several later figures are organized in the same way. Four important dynamical quantities are depicted here: (1) the local K entropy accumulated during a trajectory segment, K; (2) $\langle K_\omega \rangle$, which is the average over a trajectory segment of the K-entropy estimate K_ω of Wales and Berry; (3) the average temperature, $\langle T \rangle$; and (4) the average vibrational coupling, $\langle C \rangle$. For each of these quantities, four probability distributions are shown. The topmost distribution is that for trajectory segments in the LJ_3 potential well; underneath it are shown (in order) distri-
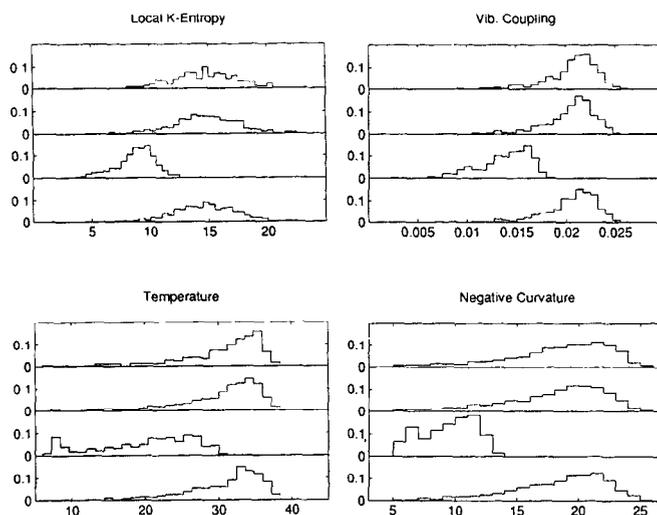

FIG. 2. Probability distributions for the local K entropy, $\langle K_\omega \rangle$, temperature, and mean vibrational coupling $\langle C \rangle$ for various trajectory segments for a LJ_3 cluster at total energy $E = -1.85$ ϵ. Each probability distribution is normalized to an area of one. The saddle-region distributions are computed from a sample of 544 saddle crossings, and the well-region distributions are computed from a sample of 525 trajectory segments in the LJ_3 potential well. Units for the abcissas are: local K entropy and $\langle K_\omega \rangle$, bits/10^{-11} s; temperature, degrees kelvin; vibrational coupling, 10^{14} s^{-1}.

butions for trajectory segments which precede a saddle crossing, for segments which include a saddle crossing, and for segments which follow a saddle crossing. All of the trajectory segments represented in these distributions are taken from MD trajectories with total energy $E = -1.85$ ϵ.

To be more precise, we use the notation introduced in Sec. II. Take the four probability distributions for the local K entropy shown in the upper left portion of Fig. 2. From top to bottom, these distributions correspond to $K^W_{3 \times 500}$, $K^{-3}_{3 \times 500}$, $K^0_{3 \times 500}$, and $K^3_{3 \times 500}$. While the local K entropy is defined only for an entire trajectory segment, the other three quantities we show in this figure are defined at each time step in a segment. Hence the distributions shown for the temperature are, from top to bottom, those for $\langle T \rangle^W_{3 \times 500}$, $\langle T \rangle^{-3}_{3 \times 500}$, $\langle T \rangle^0_{3 \times 500}$, and $\langle T \rangle^3_{3 \times 500}$; the angle brackets denote averaging over a trajectory segment, as discussed in Sec. II. Note that the well-region and saddle-region distributions are actually computed from two separate MD trajectories, and that each distribution has been normalized to unit area regardless of the number of points in the sample.

Now that we have described how Fig. 2 is organized, we will discuss its meaning. The figure shows that those MD trajectory segments which contain a saddle crossing (represented by the third histogram in each set in the figure) are dynamically very different both from those trajectory segments which either precede or follow a saddle crossing, and from those segments which reside in the LJ_3 potential well. We note that the special character of the saddle-region distributions is consistent with the view underlying transition state theory, namely that we can speak of a relatively distinct (although perhaps short-lived) state

between reactants and products with its own partition function.

Figure 2 shows that trajectory segments which contain a saddle crossing have considerably lower values of the local K entropy than do the other portions of the MD trajectory, indicating that the cluster becomes less chaotic in the saddle region. This observation agrees with our earlier results.[23] We previously suggested that the decrease in chaos in the saddle region of LJ_3 resulted from the geometry of the potential surface near the saddle point. Specifically, we suggested that the saddle region acted to "channel" neighboring phase space trajectories together, thereby preventing divergence of nearby trajectories and reducing the K entropy accumulated by the cluster in the saddle region. The data shown in Fig. 2, however, indicate that we can also view the decrease in the local K entropy in the saddle region as a relative *increase* in the degree to which the cluster undergoes regular or quasiperiodic motion in that portion of the potential energy surface. The probability distributions for the mean vibrational coupling $\langle C \rangle$ provide evidence for this point of view. We see from Fig. 2 that the trajectory segments which include a saddle crossing have substantially lower values of $\langle C \rangle$ than do the other portions of the trajectory. Hence in the saddle region the LJ_3 cluster behaves approximately like a set of three uncoupled oscillators, and the cluster's motion becomes fairly regular. This temporary (and incomplete) quasiperiodicity manifests itself in the low values of the local K entropy in the saddle region.

We also see from Fig. 2 that those trajectory segments which contain a saddle crossing have a lower average kinetic energy than the other segments. This is just what we expect for a constant-energy simulation, as the cluster's potential energy is higher at the saddle point than in the potential well. This observation, however, may lead a skeptical reader to suggest that LJ_3 exhibits less chaos in the saddle region simply because the cluster has less kinetic energy there. While we believe these trends are related, as we will discuss later, we think that the decrease in chaos near the saddle point is not simply a kinetic energy effect, and in fact is intimately related to the decoupling of the cluster's vibrational modes as measured by $\langle C \rangle$.

To see this, we examine the individual coupling elements $\{b_{jk}\}$ which are averaged to give us the mean vibrational coupling $\langle C \rangle$. (This is feasible for LJ_3 because there are only three coupling elements to examine. For a four-atom cluster, however, there are already 15 individual coupling elements $\{b_{jk}\}$.) Figure 3 shows how these coupling elements evolve in time during a representative pass over the saddle point. Here, we plot the magnitudes of the coupling elements $|b_{12}|$, $|b_{13}|$, and $|b_{23}|$ as functions of time. We also plot the cluster's kinetic energy and maximum internal angle as functions of time, in order to track its progress across the saddle point. The figure is divided horizontally into three sections of 1500 time steps each; the saddle crossing occurs in the center section, at the point where the cluster's bending angle $\theta = 180°$.

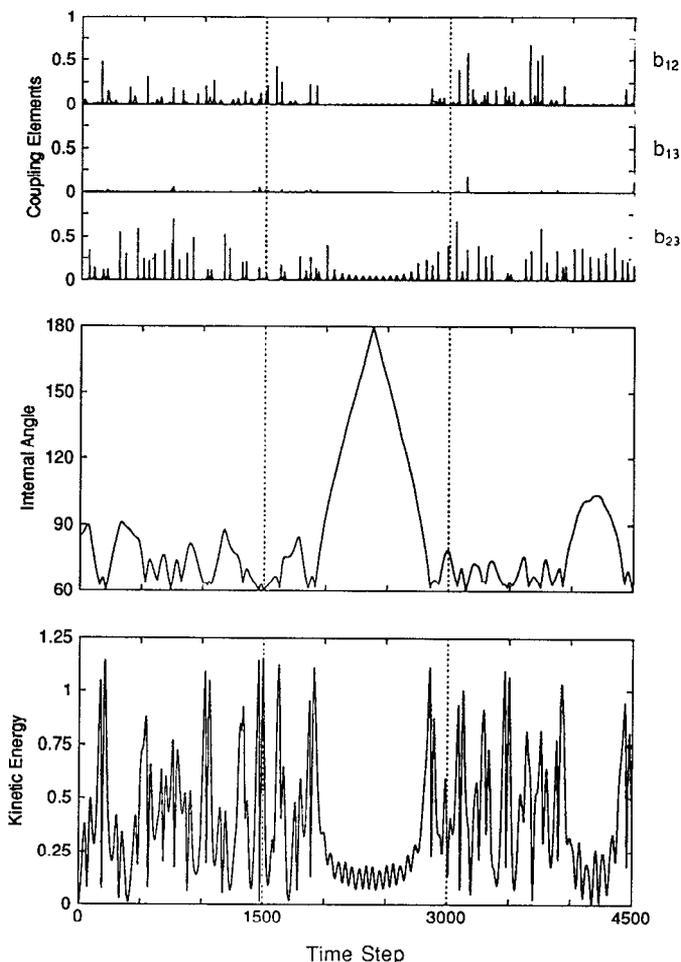We see that the coupling elements b_{12} and b_{23} behave very differently depending on whether the LJ_3 cluster is in

FIG. 3. The magnitudes of the coupling elements $|b_{12}|$, $|b_{13}|$, and $|b_{23}|$ as functions of time for a single isomerization of LJ_3. The x axis measures progress along the trajectory in units of the time step $\Delta t = 10^{-14}$ s. Also plotted as functions of time are the cluster's largest internal angle in degrees, θ, and the instantaneous kinetic energy of the cluster in ϵ. The total energy of the cluster is $E = -1.85 \epsilon$ in this trajectory segment.

the saddle region or not. In the left and right sections of Fig. 3 (corresponding to the trajectory segments preceding and following the saddle crossing), the coupling elements b_{12} and b_{23} vary rapidly with time, exhibiting several sharp peaks. In the center section of the figure, however, there is a portion of the trajectory where b_{12} and b_{23} decrease sharply in magnitude, and where b_{23} undergoes more gentle, almost periodic oscillations. From the plot of the bending angle θ, we find that this portion of the trajectory corresponds exactly to the cluster's passage across the saddle point.

Equation (1) shows that if the frequencies of two vibrational modes $\hat{u}_j$ and $\hat{u}_k$ become nearly degenerate, the corresponding coupling element b_{jk} becomes quite large. This is why b_{12} and b_{23} exhibit sharp spikes at some points. Because at each time step we sort our vibrational modes in order of increasing frequency, the opportunities for such peaks are limited to those coupling elements which couple "adjacent" pairs of modes $\hat{u}_j$ and $\hat{u}_{j+1}$. We can see a sharp peak in b_{13} only when all three modes of LJ_3 become nearly degenerate, which happens rarely in our trajectories. In

fact, modes $\hat{u}_1$ and $\hat{u}_3$ are so widely separated in frequency that the coupling element b_{13} remains very small most of the time, as Fig. 3 shows.

The behavior of the coupling elements $\{b_{jk}\}$ indicates that the vibrational modes of LJ_3 become substantially decoupled near the bending saddle point. Of particular interest is the fact that mode $\hat{u}_1$ appears to become almost completely decoupled from the other two modes. Recall that at each instant, mode $\hat{u}_1$ is defined as the vibrational mode with the lowest squared frequency ω_1^2; near the saddle point, this mode corresponds to the direction along which the potential surface has negative curvature.[34] This direction is of course the reaction coordinate for isomerization. Hence Fig. 3 shows that in the saddle region of LJ_3, motion along the isomerization coordinate is almost completely decoupled from the cluster's other degrees of freedom. (Although we have depicted only a single saddle crossing in Fig. 3, the behavior presented there is representative of LJ_3 isomerizations in general.)

Figure 3 also shows that the increase in regular behavior in the saddle region of LJ_3 is not solely a result of the low kinetic energy there. This is shown by the markedly different time dependence of the coupling elements b_{12} and b_{23} in the saddle region. If the magnitudes of the coupling elements $\{b_{jk}\}$ were determined simply by the cluster's kinetic energy, we would expect that both b_{12} and b_{23} would exhibit small but finite peaks in the center portion of Fig. 3, because the cluster's kinetic energy decreases there but remains positive. The fact that only b_{23} exhibits these peaks, while b_{12} drops to nearly zero, indicates that the decoupling of mode $\hat{u}_1$ and the consequent increase in regular or quasiperiodic motion in the saddle region is an inherent feature of the shape of the potential surface near the saddle, and is not simply due to the decrease in kinetic energy in the saddle region.

To probe more deeply into the question of mode separability near the LJ_3 bending saddle, we turn to an action-angle approach. Let the vectors $\mathbf{q}(t) = (q_{1x}, q_{1y}, ..., q_{Nz})^T$ and $\mathbf{p}(t) = (p_{1x}, p_{1y}, ..., p_{Nz})^T$ represent the instantaneous atomic positions and momenta of the cluster. We define an approximate action for mode $\hat{u}_j$ as follows:

$$I_j(n\Delta t) = \sum_{k=1}^{n} p_j(k\Delta t)\Delta q_j(k\Delta t),$$

where p_j and Δq_j are the components of the atomic momenta and displacements projected onto mode $\hat{u}_j$:

$$p_j(t) = \hat{u}_j^T(t) \cdot \mathbf{p}(t),$$

$$\Delta q_j(t) = \hat{u}_j^T(t) \cdot [\mathbf{q}(t) - \mathbf{q}(t-\Delta t)].$$

We set $I_j(t=0) = 0$ for each mode. For an isolated bound oscillator, the parametric curves $(p(t), q(t))$ are closed curves which retrace the same points during each oscillation; the associated action $I = \oint p\,dq$ is a constant of the motion. The extent to which our approximate mode actions I_j mimic this behavior is an indication of how separable the cluster's modes are.

Figure 4 shows I_3 as a function of time for the LJ_3 saddle crossing depicted earlier in Fig. 3. If we view the center portion of the trajectory on a magnified scale [Fig. 4(b)], we can see clear steplike behavior in I_3. Each short plateau in this section corresponds to a classical turning point for the mode $\hat{u}_3$, where the trajectory passes through the $p_3 = 0$ plane; hence two consecutive plateaus correspond to a complete oscillation along $\hat{u}_3$. To make this concept more precise, we define a "complete oscillation" along the mode $\hat{u}_j$ as a portion of the MD trajectory terminated at both ends by points where p_j changes from positive to negative. This definition permits us to apply the term "oscillation" to other portions of the trajectory where steplike behavior in I_3 may be less obvious. In Fig. 4(b), we have indicated with arrows the end points of several complete oscillations along $\hat{u}_3$. The increase in I_3 during a single complete oscillation, ΔI_3, is the quantity which corresponds to the true action $I = \oint p\,dq$, and which should be constant for a completely decoupled oscillator.

Table I shows that ΔI_3 is in fact fairly well conserved during the saddle crossing. During the six complete oscillations along mode $\hat{u}_3$ which occur between steps 2029 and 2712 [those marked in Fig. 4(b)], ΔI_3 remains between $0.2575h$ and $0.2775h$; this is a very narrow range when compared with the fluctuations in ΔI_3 for the oscillations preceding and following this portion of the MD trajectory. Table II shows that ΔI_2 is not conserved quite as well during the isomerization: we see that between steps 2001 and 2740, which correspond to 13 oscillations along $\hat{u}_2$, ΔI_2 fluctuates within the somewhat larger interval $0.0034h < \Delta I_2 < 0.042h$. This interval is still rather narrow, however, when compared with the fluctuations in ΔI_2 preceding and following the saddle crossing. We have examined several other isomerizations of LJ_3 which are not shown here; during each isomerization, ΔI_2 and ΔI_3 are fairly well conserved in the saddle region. We find that these actions are generally conserved best when they fluctuate around an average value greater than about $0.1h$.

Tables I and II also indicate that the periods of the oscillations along modes $\hat{u}_2$ and $\hat{u}_3$ remain roughly constant as the cluster traverses the bending saddle. This observation leads us back to the plots of $|b_{jk}|$ shown in Fig. 3. We see that the sharp spikes in $|b_{12}|$ and $|b_{23}|$ found in the left and right portions of this figure occur at apparently random intervals, while the more gentle oscillations in $|b_{23}|$ at the center of Fig. 3 are much more periodic, reflecting the nearly quasiperiodic behavior of the cluster in the saddle region.

The only exception to this pattern is near the right edge of Fig. 3; between steps 4000 and 4350 we see six nearly periodic spikes in $|b_{23}|$. (The actual locations of the spikes are steps 4011, 4076, 4139, 4207, 4267, and 4339,
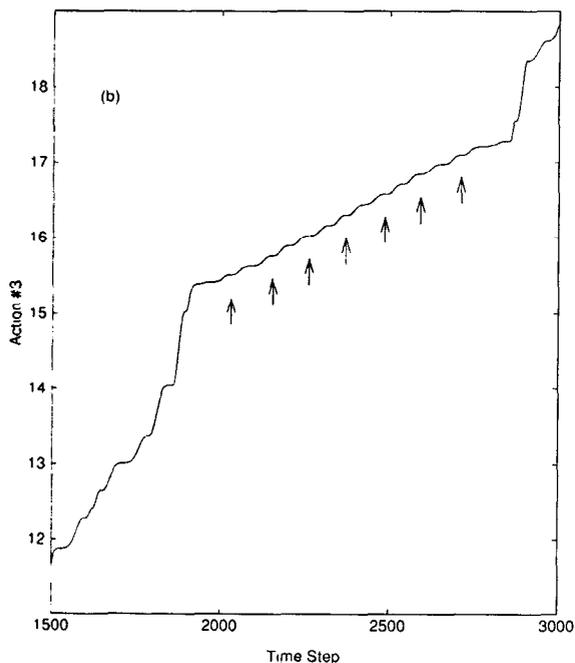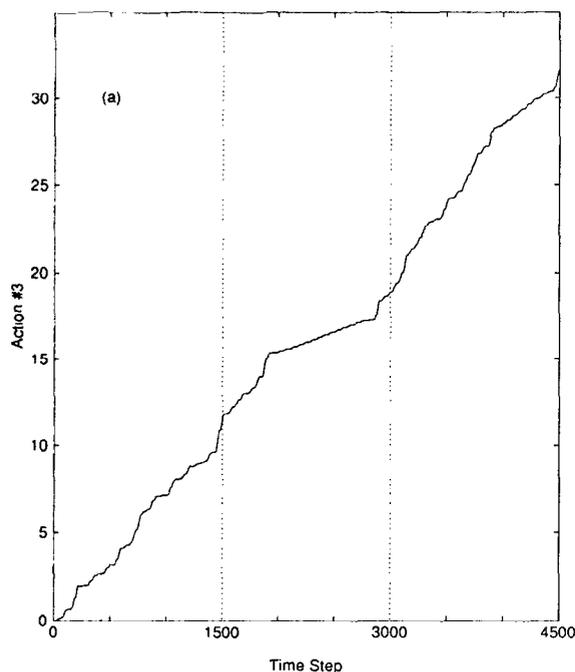
TABLE I. The periods and increases in action for those complete oscillations along mode $\hat{u}_3$ which take place during the middle third (steps 1500–3000) of the trajectory shown in Figs. 3 and 4. ΔI_3 is given in multiples of Planck's constant h.

Initial and final time steps	Period (time steps)	ΔI_3
1434–1526	92	2.240
1526–1622	96	0.532 5
1622–1713	91	0.601 1
1713–1853	140	1.028
1853–1933	80	1.349
1933–2029	96	0.119 0
2029–2153	124	0.257 5
2153–2262	109	0.263 1
2262–2371	109	0.271 8
2371–2486	105	0.277 5
2486–2591	105	0.261 1
2591–2712	121	0.259 5
2712–2809	97	0.136 5
2809–2854	45	0.045 47
2854–2906	52	1.055
2906–2986	80	0.334 8
2986–3056	70	0.719 1

quasiperiodic dynamics. The critical bending angle beyond which mode $\hat{u}_1$ becomes largely decoupled seems to be approximately $\theta = 90°$.

From the evidence presented in Figs. 3 and 4, we conclude that the vibrational Hamiltonian of LJ$_3$ becomes largely separable when the cluster is near the bending saddle. This separability manifests itself not only in the coupling constants $\{b_{jk}\}$ and the mode actions I_j, but also in the local K entropy of the cluster, which decreases substan-

FIG. 4. (a) Time dependence of the approximate mode action $I_3(t)$ for the LJ$_3$ saddle crossing depicted in Fig. 3. The x axis measures time in units of the time step $\Delta t = 10^{-14}$ s. I_3 is measured in multiples of Planck's constant h. (b) Expanded view of the center portion of $I_3(t)$. Arrows mark the end points of six complete oscillations along mode $\hat{u}_3$.

giving an average spacing of 66 ± 6 time steps.) From the plot of θ we see that in this part of the trajectory, the cluster enters the saddle region but is reflected out before it crosses the saddle. Nevertheless, the cluster has penetrated deeply enough into the saddle region to effectively decouple mode $\hat{u}_1$, as $|b_{12}|$ becomes quite small during this interval. This portion of the trajectory also shows steplike behavior in the actions I_2 and I_3, which is characteristic of

TABLE II. The periods and increases in action for those complete oscillations along mode $\hat{u}_2$ which take place during the middle third (steps 1500–3000) of the trajectory shown in Figs. 3 and 4. ΔI_2 is given in multiples of Planck's constant h.

Initial and final time steps	Period (time steps)	ΔI_2
1451–1628	177	1.214
1628–1824	196	1.004
1824–1918	94	0.738 2
1918–2001	83	0.117 6
2001–2056	55	0.016 44
2056–2126	70	0.041 98
2126–2177	51	0.009 604
2177–2227	50	0.013 47
2227–2298	71	0.020 51
2298–2348	50	0.010 68
2348–2392	44	0.003 784
2392–2456	64	0.017 18
2456–2518	62	0.018 85
2518–2563	45	0.003 460
2563–2622	59	0.019 29
2622–2687	65	0.032 61
2687–2740	53	0.009 617
2740–2837	97	0.116 5
2837–3043	106	1.950 0

tially in the saddle region. We next ask if there are any simple geometric or topological features of the potential energy saddle which are responsible for this near-separability. This leads us back to Fig. 2, and specifically to the probability distributions for $\langle K_\omega \rangle$.

Figure 2 clearly shows that the saddle segments of the MD trajectory of LJ_3 exhibit $\langle K_\omega \rangle$ values which are substantially different from those in the other types of trajectory segments. Recall that K_ω varies in tandem with the instantaneous negative curvature of the potential surface. Although each of the four types of MD trajectory segments typically experiences some negative curvature, the areas of the potential surface explored by saddle segments have less negative curvature than those areas explored by other trajectory segments. This is consistent with our earlier observations on LJ_3 and M_3 clusters.[23] Originally, Wales and Berry[27] intended that $\langle K_\omega \rangle$ would serve as a computationally inexpensive estimate of the true K entropy; we see from Fig. 2 that although the absolute magnitudes of K and $\langle K_\omega \rangle$ are not particularly close, these two measures follow similar trends. (The predictive value of K, $\langle K_\omega \rangle$, and other related estimates of the true global K entropy is discussed in more detail elsewhere.[18,19,23,27,35])

At first it may seem puzzling that the LJ_3 cluster encounters more negative curvature in the potential well than near the saddle point, or even that there is substantial negative curvature in the potential minimum at all. While there is by definition at least one imaginary vibrational frequency ω_{sad} at a saddle, in LJ_3 the magnitude of that frequency, which is associated with the bending mode of the linear configuration, is quite small: $\omega_{sad} = 7.32i$ cm^{-1}. At the high energy considered here ($E = -1.85\ \epsilon$), a LJ_3 trajectory segment which remains within the potential well probably spends a large fraction of time high on the sides of the well, where there is substantial negative curvature in the cluster's stretching modes. This stretching negative curvature is often larger in magnitude than the very gentle negative curvature associated with the bending mode near the saddle point. Hence the cluster on average experiences more negative curvature in the well than in the saddle region, which is comparatively flat along directions of negative curvature.

In addition, we find that in LJ_3, the flat saddle is efficient at decoupling a cluster's vibrational modes and inducing approximately quasiperiodic behavior; this will prove to be true for three-atom Morse clusters as well, and to a limited extent for LJ_4. This seems plausible if we consider the two extreme cases of a very flat saddle with almost no negative curvature along the isomerization coordinate, and a very sharp saddle that is markedly pinched. As a physical model for these saddles, we might imagine an hourglass whose neck can be stretched or compressed by pulling or pushing on the two globes at either end. An hourglass with a long neck obviously corresponds to a flat saddle, while a short-necked hourglass contains a saddle which is sharply negatively curved.

In the case of the flat saddle, the shape of the potential surface changes very slowly along the reaction coordinate; hence the vibrational mode corresponding to isomerization should become largely decoupled from the other modes. In the case of the sharply pinched saddle, however, the interaction between the saddle-crossing mode and any other mode which may couple to it is enhanced because the shape of the potential surface changes rapidly along the reaction coordinate. Hence we expect that, in general, the vibrational decoupling in a saddle region (and therefore the degree of quasiperiodicity there) should vary with the flatness of the saddle.

This qualitative argument is admittedly rather crude; for example, it ignores both the effects of reaction path curvature and the possibility that the sides of a saddle may ripple in and out as the reaction path is traversed. However, it seems that in our clusters, these effects are usually less important than the flatness of a given saddle. When we discuss five-atom Morse clusters, for example, we will find that there is no significant rippling of the saddle walls, and that the negative curvatures in the saddle region are the primary determinant of the clusters' dynamics there.

This argument also helps explain the correlation between the decrease in local K entropy near the saddle and the decrease in kinetic energy there. Because flatter saddles are naturally longer in the direction of the isomerization coordinate, we expect that trajectory segments in flat saddle regions will be substantially colder than "well" segments with the same total energy. Conversely, trajectory segments which pass over a sharply pinched (hence shorter) saddle will sample a high-potential-energy region of the surface for only a short time, and may be only slightly colder than corresponding "well segments."

We conclude our discussion of Fig. 2, and of the LJ_3 cluster, by mentioning that for each of the four quantities shown in this figure, the probability distributions for segments preceding and following the saddle crossing are quite similar both to each other, and to the probability distribution for segments residing in the potential well. This similarity is not merely qualitative: Table III shows that for each of the four quantities studied, the means of these three distributions are very close. In fact, according to the Kolmogorov–Smirnov test[36] and to Student's t test for paired samples,[36] these three distributions are statistically indistinguishable for each of the four quantities shown. (We test for statistical significance at the 1% level throughout this article.) We can draw two important conclusions from this observation.

First, the cluster's dynamics are essentially the same for segments preceding and following an isomerization. This is just what we expect for a symmetric saddle because the cluster's equations of motion are microscopically reversible in time. We can therefore conclude that there is no "memory" of the cluster having passed over a saddle, which confirms the validity of a local interpretation[27] of the chaotic dynamics in LJ_3. Second, we see that at this energy ($-1.85\ \epsilon$), the saddle crossing takes place quickly enough so that there is little difference between 1500-step trajectory segments in the potential well and segments either preceding or following an isomerization. We originally distinguished between "well" segments and segments immediately preceding or following an isomerization because

TABLE III. Comparison of the means of the probability distributions for K, $\langle K_\omega \rangle$, $\langle T \rangle$, and $\langle C \rangle$ for LJ$_3$ as shown in Fig. 2 and for $\rho=6$ and $\rho=3$ M$_3$ as shown in Figs. 5 and 6. Units are the same as those for the abcissas in the figures.

Quantity	Mean for LJ$_3$	Mean for M$_3$ $\rho=6$	Mean for M$_3$ $\rho=3$
$K_{3\times500}^W$	14.54	14.50	8.48
$K_{3\times500}^{-3}$	14.67	14.72	8.48
$K_{3\times500}^0$	8.75	8.49	7.27
$K_{3\times500}^{+3}$	14.60	14.55	8.49
$\langle K_\omega \rangle_{3\times500}^W$	18.48	17.77	10.23
$\langle K_\omega \rangle_{3\times500}^{-3}$	18.12	17.68	10.16
$\langle K_\omega \rangle_{3\times500}^0$	9.43	9.18	7.67
$\langle K_\omega \rangle_{3\times500}^{+3}$	18.39	17.59	10.31
$\langle T \rangle_{3\times500}^W$	30.54	32.70	34.37
$\langle T \rangle_{3\times500}^{-3}$	30.54	32.97	33.73
$\langle T \rangle_{3\times500}^0$	19.93	19.72	29.36
$\langle T \rangle_{3\times500}^{+3}$	30.71	32.98	34.28
$\langle C \rangle_{3\times500}^W$	0.0207	0.0201	0.0117
$\langle C \rangle_{3\times500}^{-3}$	0.0205	0.0200	0.0115
$\langle C \rangle_{3\times500}^0$	0.0138	0.0131	0.0095
$\langle C \rangle_{3\times500}^{+3}$	0.0206	0.0201	0.0118

FIG. 5. Probability distributions similar to those given in Fig. 2, except for a M$_3$ cluster with $\rho=6$ and at total energy $E=-1.85\ \epsilon$. The saddle-region distributions are computed from a sample of 522 saddle crossings, and the well-region distributions are computed from a sample of 708 trajectory segments in the M$_3$ potential well. Units for the abcissas are as in Fig. 2.

we thought that the latter segments might show dynamical behavior intermediate between that of the saddle and well regions. This is not the case for LJ$_3$, and Fig. 3 shows why: for the isomerization shown there, the entire saddle crossing takes only 900 time steps, so that the isomerization event easily fits within a 1500-step "saddle segment." Furthermore, the cluster's dynamics on either side of the saddle are dominated by rapid vibrations within a single well.

In principle, we could determine more precisely how sharp the transition from well-like to saddlelike dynamics is by reducing our quench interval and repeating the calculations summarized in Fig. 2. However, we can obtain essentially the same information from the time dependence of $|b_{23}|$ shown in Fig. 3. This plot shows that at the energy $E=-1.85\ \epsilon$, the transition takes place in less than 100 time steps. Hence to obtain any quantitative information about the transition from well-like to saddlelike dynamics, we must reduce our quench interval to less than 100 steps, which is computationally impractical. In addition, if we divide our trajectory into such short segments and retain the current algorithm, the intrinsic variation in the duration of the isomerization process might obscure any behavior specific to the well-to-saddle transition region.

B. M$_3$ clusters

Next, we discuss a similar body of results for two different three-atom Morse clusters. The two clusters we discuss here differ only in their values of the range parameter ρ: one cluster has $\rho=6$, which corresponds to a Morse pair potential whose range is comparable to a Lennard-Jones potential, while the other cluster has $\rho=3$, which corresponds to a Morse potential substantially longer in range. We have chosen these values of ρ to facilitate comparison with our previous work on three-atom clusters. We emphasize that for both of these clusters, the potential energy
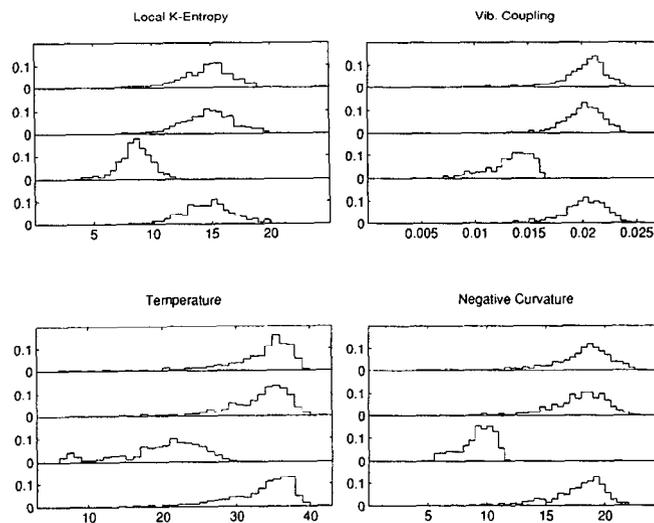
surface has the same general structure as that of LJ$_3$. The energy of the equilateral triangle minimum is $E=-3.00\ \epsilon$ for both M$_3$ clusters; the saddle point has energy $E=-2.005\ \epsilon$ for the $\rho=6$ cluster and energy $E=-2.102\ \epsilon$ for the $\rho=3$ cluster.

First, we present our results for the shorter range potential. Figure 5 shows several probability distributions like those in Fig. 2, but calculated for a M$_3$ cluster with $\rho=6$ instead of for a Lennard-Jones cluster. The results for this cluster are qualitatively very similar to those shown earlier for LJ$_3$: those segments of the cluster's MD trajectory in the saddle region are substantially colder and less chaotic than trajectory segments on other parts of the potential surface. Saddle-region segments also encounter less vibrational mode coupling and less negative curvature, as measured by $\langle C \rangle$ and $\langle K_\omega \rangle$, respectively. It is not surprising that the dynamics of this cluster are similar to those of LJ$_3$, because the Lennard-Jones pair potential and the $\rho=6$ Morse potential are quite similar.

However, the M$_3$ cluster bound by long-range Morse pair potentials (with $\rho=3$) behaves quite differently. In Fig. 6, we show probability distributions for the same four dynamical quantities—K, $\langle K_\omega \rangle$, $\langle T \rangle$, and $\langle C \rangle$—for a three-atom Morse cluster with $\rho=3$. We notice that in this cluster, the differences between the saddle-region distributions and those distributions computed from segments exploring other portions of the potential surface are much less pronounced. Table III compares the means of the distributions for the LJ$_3$ cluster and the $\rho=3$ and $\rho=6$ M$_3$ clusters; we see that although the saddle region in the $\rho=3$ cluster still acts to decouple the cluster's vibrational modes, and therefore reduces the local K entropy accumulated near the saddle, this effect is not as strong as in either the $\rho=6$ Morse cluster or the Lennard-Jones cluster.

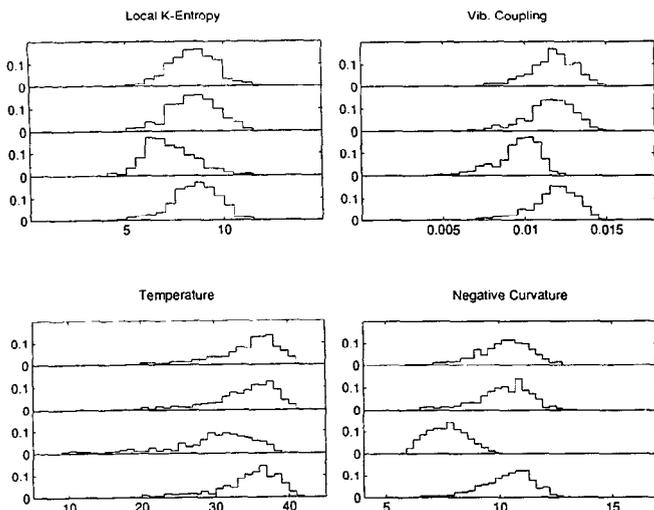This qualitative difference between three-particle clus-

FIG. 6. Probability distributions similar to those given in Fig. 5, except for a M_3 cluster with $\rho=3$ and at total energy $E=-1.85\ \epsilon$. The saddle-region distributions are computed from a sample of 531 saddle crossings, and the well-region distributions are computed from a sample of 562 trajectory segments in the M_3 potential well. Units for the abcissas are as in Fig. 2.

FIG. 7. Probability distributions similar to those given in Fig. 2, except for a LJ_4 cluster at total energy $E=-4.5\ \epsilon$. The saddle-region distributions are computed from a sample of 683 saddle crossings, and the well-region distributions are computed from a sample of 547 trajectory segments in the potential well. Units for the abcissas are as in Fig. 2.

ters bound by short-range potentials and those bound by long-range potentials agrees well with our earlier work,[23] and is just what we might predict from the argument we outlined above relating the flatness of the LJ_3 saddle to its ability to decouple a cluster's vibrational modes. In the $\rho=6\ M_3$ cluster, as in the Lennard-Jones cluster, MD trajectory segments which pass over the saddle tend to explore regions of the potential surface which are considerably flatter than those portions of the trajectory in the potential well; as we explained earlier, this leads to good separation of the vibrational modes in the saddle region. In the $\rho=3$ Morse cluster, however, the negative curvature sampled by trajectory segments in the saddle region (as measured by $\langle K_\omega \rangle$) is only slightly less than that sampled by well-region segments, so the decoupling is less effective in the saddle region of this cluster.

We can locate the origin of this behavior in the shape of the potential surfaces of these clusters at their respective saddle points. Recall that we found that the saddle region in LJ_3 is very flat in the negatively curved direction, with $\omega_{sad}=7.32i\ cm^{-1}$. The saddle of the M_3 cluster with $\rho=6$ is even flatter, with $\omega_{sad}=4.14i\ cm^{-1}$; the saddle of the $\rho=3\ M_3$ cluster, on the other hand, is more pinched, with $\omega_{sad}=13.48i\ cm^{-1}$. Hence we can begin to formulate a general principle which permits us to understand a cluster's dynamics in terms of the shape of its potential energy saddles, and which encompasses both Lennard-Jones and Morse clusters. That principle is that flat saddles which prevail in clusters bound by short-range potentials tend to be less effective at "defocusing" MD trajectories, and also act to induce vibrational decoupling in small clusters. These two effects increase the relative degree of quasiperiodic behavior near the saddle point and reduce the local K entropy there.

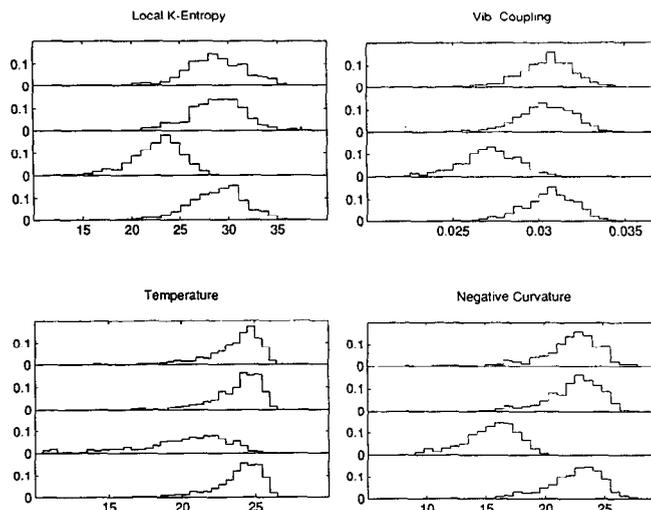Table III also provides further evidence that the trends

in the local K entropy we observe for three-atom clusters primarily reflect the degree of vibrational coupling and negative curvature near the saddle, and not the kinetic energy of the clusters. For example, we find that in all regions of the potential surface, the $\rho=3\ M_3$ cluster is both substantially hotter and considerably less chaotic than the LJ_3 cluster; this is because the vibrational modes of the Morse cluster are coupled more weakly, as measured by $\langle C \rangle$, despite the higher kinetic energy in that cluster. Similarly, for MD trajectory segments in the potential well, the $\rho=6\ M_3$ cluster is somewhat hotter than LJ_3; however, these two clusters have roughly equal values of $\langle C \rangle$ and $\langle K_\omega \rangle$ in the well, and hence comparable degrees of chaos there.

C. LJ_4 clusters

Next, we present our results for the four-atom Lennard-Jones cluster; we will find that this cluster as well fits into the general principle outlined above. The LJ_4 cluster, like LJ_3, has a fairly simple potential energy surface with only one kind of minimum and one kind of first-rank saddle point. The minimum corresponds to a tetrahedral configuration of the atoms, and has energy $E=-6.00\ \epsilon$; the saddle point corresponds to a planar rhombus-shaped cluster, and has energy $E=-5.073\ \epsilon$. (The square planar cluster, with $E=-4.481\ \epsilon$, is also a stationary point of the potential surface, but it is a second-rank saddle, with two imaginary vibrational frequencies of $23.13i\ cm^{-1}$ and $43.56i\ cm^{-1}$.)

In Fig. 7 we show the by-now familiar probability distributions, computed at $E=-4.5\ \epsilon$, for the local K entropy, $\langle K_\omega \rangle$, temperature, and vibrational coupling for trajectory segments in different regions of the LJ_4 potential surface. We see that LJ_4 behaves similarly to LJ_3: the saddle-region segments stand out as substantially colder
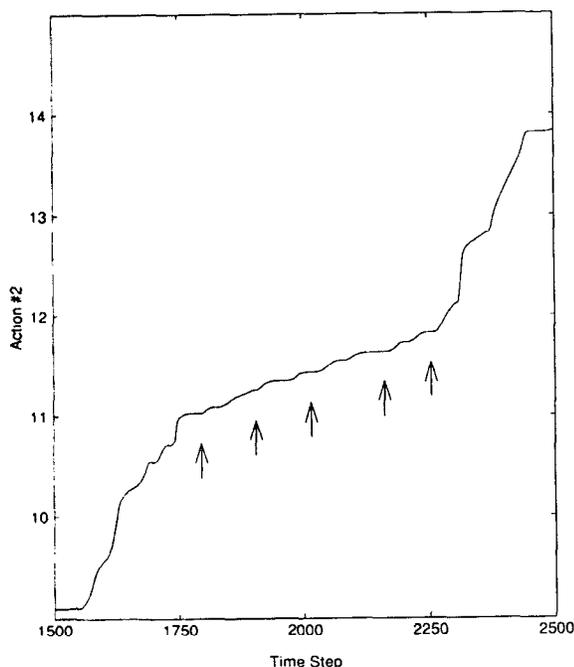
FIG. 8. Time dependence of the approximate mode action $I_2(t)$ for a single LJ_4 saddle crossing. The x axis measures time in units of the time step $\Delta t = 10^{-14}$ s; the actual isomerization takes place between steps 1750 and 2300. I_2 is measured in multiples of Planck's constant h. Arrows mark the end points of four complete oscillations along mode $\hat{u}_2$ during the isomerization.

TABLE IV. Energies (in ϵ) and imaginary vibrational frequencies (in cm^{-1}) for LJ_5 and M_5 clusters at their respective stationary points.

	LJ_5	$\rho=5$ M_5	$\rho=9$ M_5
Minimum			
$E=$	-9.104	-9.085	-9.007
DSD saddle			
$E=$	-8.481	-8.497	-8.096
$\omega_{sad}=$	$35.52i$	$39.44i$	$30.31i$
EB saddle			
$E=$	-8.198	-8.161	-8.011
$\omega_{sad}=$	$18.84i$	$20.99i$	$8.64i$

and less chaotic than trajectory segments in any other region of the surface; they also sample areas of the potential surface which are less negatively curved and which couple the cluster's modes together less strongly. As in LJ_3, this dynamical behavior reflects in part the fact that the saddle region in LJ_4 is fairly flat along the isomerization coordinate, with $\omega_{sad}=10.59i$ cm^{-1}. We should also point out that, as in LJ_3, the dynamics of LJ_4 are essentially the same for trajectory segments preceding and following an isomerization (as expected from considerations of microscopic reversibility), and that these segments are statistically indistinguishable from those segments which remain in the potential minimum.

We have performed an action-angle analysis of the vibrational modes of LJ_4 like that described above for LJ_3. We find that in the four-atom cluster, the individual mode actions in the saddle region are not conserved as well as in LJ_3. Only the action corresponding to mode $\hat{u}_2$ generally shows clear steplike behavior during the isomerization process; this is indicated for a representative saddle crossing in Fig. 8. For the four complete oscillations along mode $\hat{u}_2$ marked with arrows in this figure, ΔI_2 varies between $0.178h$ and $0.228h$. This range is somewhat larger than the corresponding ranges for ΔI_2 and ΔI_3 in the saddle region of LJ_3 (Tables I and II). Because the saddle in LJ_4 is not quite as flat as that in LJ_3, and therefore gives rise to larger values of $\langle C \rangle$ and the local K entropy in the saddle region of LJ_4, we naturally expect that the saddle-region mode actions will be less well conserved in LJ_4. Nevertheless, we

were surprised to find that only mode $\hat{u}_2$ maintained a roughly constant action in the saddle region.

We can think of two possible explanations for this observation. It may be that as we increase the size of our cluster, the newly added vibrational modes "pile up" in a relatively narrow range of high vibrational frequencies; these modes would then couple more effectively with each other because of their near-degeneracy, and any approximately quasiperiodic motion of the cluster would be confined to the lowest frequency modes. In addition, as we increase the number of modes in a cluster, we may observe the onset of a "dynamical size effect": by this, we mean that in systems with many degrees of freedom, the influence of any one "special" degree of freedom (such as the isomerization coordinate) may become obscured or unimportant. These two possibilities are not mutually exclusive: the "piling-up" of vibrational frequencies may be the first stage in the onset of a dynamical size effect. These conjectures deserve further exploration.

D. LJ_5 clusters

Next, we discuss the LJ_5 cluster, which has only one kind of minimum but has two different kinds of first-rank saddle points. In the first column of Table IV we summarize the energies of these stationary points and the imaginary vibrational frequencies of the two saddles. The lower saddle connects two permutational isomers of the LJ_5 cluster by a diamond–square–diamond[37] (DSD) pathway, while the higher saddle connects two LJ_5 isomers by an edge-bridging[38] (EB) pathway. Our technique for isolating saddle-crossing trajectory segments is able to distinguish between these two saddles because they connect permutationally distinct *pairs* of minima; a given minimum-energy configuration of the LJ_5 cluster is transformed into two distinct labeled minima by the DSD and EB isomerizations.

We note that both saddles are considerably more pinched than those found in the LJ_3 and LJ_4 clusters. We therefore anticipate that the saddles of LJ_5 will be less effective than those of LJ_3 or LJ_4 at decoupling the cluster's vibrational modes and inducing approximate quasiperiodic behavior. This is in fact what we observe.

First, we examine the high-energy EB saddle, which with $\omega_{sad}=18.84i$ cm^{-1} is the flatter of the two saddles in
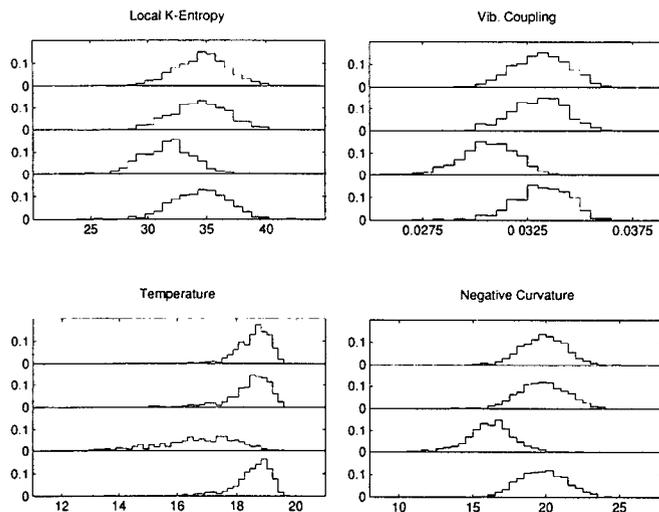
FIG. 9. Probability distributions similar to those given in Fig. 2, except for a LJ_5 cluster crossing its EB saddle at total energy $E = -7.5 \epsilon$. The saddle-region distributions are computed from a sample of 630 saddle crossings of the edge-bridging saddle, and the well-region distributions are computed from a sample of 650 trajectory segments in the potential well. Units for the abcissas are as in Fig. 2.
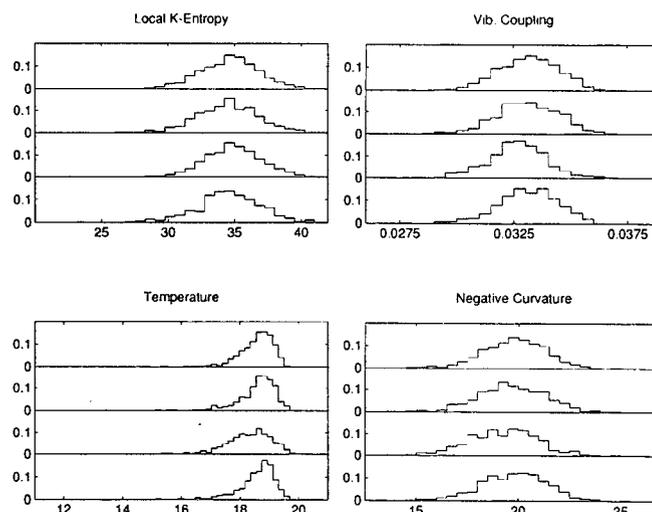
FIG. 10. Probability distributions similar to those given in Fig. 9, except for the DSD saddle of LJ_5. The saddle-region distributions are computed from a sample of 662 saddle crossings of the DSD saddle, and the well-region distributions are computed from a sample of 650 trajectory segments in the potential well. Units for the abcissas are as in Fig. 2.

the LJ_5 cluster. In Fig. 9 we give probability distributions for K, $\langle K_\omega \rangle$, $\langle T \rangle$, and $\langle C \rangle$ for a LJ_5 cluster at $E = -7.5 \epsilon$ as it crosses this saddle; the means of these distributions are summarized in the first column of Table V. We see that trajectory segments of LJ_5 which cross the EB saddle have only slightly smaller values of these four quantities than do segments in the potential well. This observation is in keeping with the trend established for three- and four-atom clusters that a cluster's dynamics are least chaotic in those areas of the potential surface with the least negative curvature.

TABLE V. Comparison of the means of the probability distributions for K, $\langle K_\omega \rangle$, $\langle T \rangle$, and $\langle C \rangle$ for the EB saddle crossings of LJ_5 (see Fig. 9) and $\rho = 5$ and $\rho = 9$ M_5 clusters (see Figs. 11 and 12), all at energies of $E = -7.5\epsilon$. Units are the same as those for the abcissas in the figures.

Quantity	Mean for LJ_5	Mean for M_5 $\rho = 5$	Mean for M_5 $\rho = 9$
$K_{3\times500}^W$	34.60	25.27	36.83
$K_{3\times500}^{-3}$	34.37	25.14	36.64
$K_{3\times500}^0$	31.59	25.08	30.17
$K_{3\times500}^{+3}$	34.41	25.18	36.53
$\langle K_\omega \rangle_{3\times500}^W$	19.80	14.23	18.03
$\langle K_\omega \rangle_{3\times500}^{-3}$	19.73	13.91	18.01
$\langle K_\omega \rangle_{3\times500}^0$	16.25	12.81	13.31
$\langle K_\omega \rangle_{3\times500}^{+3}$	19.74	14.14	18.14
$\langle T \rangle_{3\times500}^W$	18.57	18.80	18.06
$\langle T \rangle_{3\times500}^{-3}$	18.45	18.85	18.04
$\langle T \rangle_{3\times500}^0$	16.58	16.93	13.48
$\langle T \rangle_{3\times500}^{+3}$	18.50	18.83	17.96
$\langle C \rangle_{3\times500}^W$	0.0331	0.0266	0.0434
$\langle C \rangle_{3\times500}^{-3}$	0.0330	0.0266	0.0433
$\langle C \rangle_{3\times500}^0$	0.0306	0.0245	0.0370
$\langle C \rangle_{3\times500}^{+3}$	0.0332	0.0266	0.0432

However, we note that the fractional decrease in K near the EB saddle of LJ_5 is somewhat smaller than that near either the LJ_3 or LJ_4 saddle. This suggests that the EB saddle of LJ_5, because of its greater negative curvature along the isomerization coordinate, is less effective than either the LJ_3 or LJ_4 saddle at collimating the flow of saddle-crossing trajectories.

Next, we examine the DSD saddle of LJ_5; this saddle is very sharply pinched, with $\omega_{sad} = 35.52i$ cm^{-1}. In Fig. 10 we show probability distributions for K, $\langle K_\omega \rangle$, $\langle T \rangle$, and $\langle C \rangle$ for a LJ_5 cluster crossing the DSD saddle at $E = -7.5 \epsilon$. The means of these distributions are summarized in the first column of Table VI. There appears to be virtually no difference between the dynamics of the LJ_5 cluster in the DSD saddle region and in the well region. Hence we conclude that the DSD saddle of LJ_5 is completely ineffective at collimating phase space trajectories.

It is interesting to note that the differences between a cluster's dynamics in the saddle region and those in the well region seem to diminish as the saddle becomes more sharply negatively curved. There are at least two possible intepretations which are consistent with this observation. (1) As the negative curvature associated with the isomerization coordinate increases, it is plausible that the mean negative curvature experienced by trajectory segments in the saddle region approaches that experienced by well-region segments. Because it appears that the magnitude of negative curvature experienced by a trajectory segment largely determines the degree of local chaos and vibrational coupling in the segment, we expect under this scenario that for moderately sharp saddles, the dynamics characteristic of the well and saddle regions will be quite similar. (2) On the other hand, for increasingly sharp saddles we expect that MD trajectories which cross the saddle point spend less and less time "on the saddle." Hence as we increase the

TABLE VI. Comparison of the means of the probability distributions for K, $\langle K_\omega \rangle$, $\langle T \rangle$, and $\langle C \rangle$ for the DSD saddle crossings of LJ_5 (see Fig. 10) and $\rho=5$ and $\rho=9$ M_5 clusters (see Figs. 13 and 14), all at energies of $E=-7.5\epsilon$. Units are the same as those for the abcissae in the figures.

Quantity	Mean for LJ_5	Mean for M_5 $\rho=5$	Mean for M_5 $\rho=9$
$K_{3\times500}^W$	34.60	25.27	36.83
$K_{3\times500}^{-3}$	34.48	25.07	36.55
$K_{3\times500}^0$	34.90	26.54	35.39
$K_{3\times500}^{+3}$	34.54	25.21	36.53
$\langle K_\omega \rangle_{3\times500}^W$	19.80	14.23	18.03
$\langle K_\omega \rangle_{3\times500}^{-3}$	19.67	13.98	18.02
$\langle K_\omega \rangle_{3\times500}^0$	19.28	14.61	17.68
$\langle K_\omega \rangle_{3\times500}^{+3}$	19.80	14.04	17.89
$\langle T \rangle_{3\times500}^W$	18.57	18.80	18.06
$\langle T \rangle_{3\times500}^{-3}$	18.54	18.89	18.00
$\langle T \rangle_{3\times500}^0$	18.31	18.71	16.45
$\langle T \rangle_{3\times500}^{+3}$	18.53	18.88	18.06
$\langle C \rangle_{3\times500}^W$	0.0331	0.0266	0.0434
$\langle C \rangle_{3\times500}^{-3}$	0.0331	0.0266	0.0434
$\langle C \rangle_{3\times500}^0$	0.0327	0.0262	0.0409
$\langle C \rangle_{3\times500}^{+3}$	0.0331	0.0266	0.0434

sharpness of a saddle while keeping the trajectory segment length fixed, "saddle-crossing" segments include larger fractional contributions from the well region, and become less and less representative of the "true" dynamics on the saddle. In this scenario, the dynamics observed for saddle-region and well-region segments converge as the saddles sharpen simply because the "saddle-region" segments lose their special saddlelike character and look just about like well-region segments.

The essential difference between these interpretations is as follows. Under interpretation (1) the cluster can be said to have specific dynamical properties associated with the saddle region, although the dynamics near the saddle may appear similar to those associated with the potential well. Under interpretation (2), however, the concept of "saddle-region dynamics" may become largely invalid on the time scale of the MD trajectory segment.

From the data presented here, we cannot determine which of these interpretations explains the gradual convergence of well- and saddle-region dynamics in Lennard-Jones and Morse clusters as the saddles of these clusters become sharper. An additional complication is introduced by the possibility that the dynamics observed near a given saddle may correspond to interpretation (1) at low energies and interpretation (2) at high energies. This is because at energies where the cluster has just slightly more energy than is required to cross the saddle, the trajectory can spend a long enough period of time "on the saddle" to establish distinct dynamical properties associated with the saddle geometry; this is probably true for even moderately sharp saddles. At high energies, however, trajectories may pass so quickly over a saddle that we cannot observe distinct "saddle-region dynamics" on any but the shortest time scale; this may even be true for fairly flat saddles.

It may be that any given saddle has an associated "crit-

ical energy" or energy range, below which we can identify distinct saddle-region dynamics and above which we cannot; this energy (or more precisely, the excess energy above that required to cross the saddle) should be lower for sharper saddles. We expect this critical energy to be bounded from above by the energy at which t_{cross}, the cluster's transit time through the negatively curved interval of the isomerization reaction coordinate, is comparable to the longest vibrational period of the cluster's stable vibrational modes; that is, at the energy where

$$t_{cross} = s/v = s/\langle p_1 \rangle \approx 2\pi/\omega_2.$$

In this equation, s is the length of the negatively curved interval of the reaction coordinate and $v = \langle p_1 \rangle$ is the mean velocity of the cluster along the reaction coordinate in the saddle region. (Recall from Sec. III A that p_1 is the projection of the cluster's atomic momenta onto mode $\hat{u}_1$, which is the isomerization coordinate in the saddle region.) To fully understand the behavior of a cluster near a sharp saddle point, we must examine the cluster's dynamics over a range of energies; in Sec. IV we will sketch out one method for accomplishing this and will apply it to the three- and four-atom clusters studied above.

We emphasize that for all of the saddles mentioned so far except the DSD saddle in LJ_5, we have found statistically significant differences between the dynamics of 1500-step well-region and saddle-region segments; this indicates that we are below any "critical energy" at which scenario (2) might become important on this time scale for these saddles.

E. M_5 clusters

We have performed calculations similar to those summarized in Figs. 9 and 10 for two different M_5 clusters, one bound by a pair potential slightly longer in range than the Lennard-Jones potential ($\rho=5$), and one bound by a potential much shorter in range ($\rho=9$). These two clusters have potential surfaces with the same topological structure as that of LJ_5, although as Table IV shows, the energies and curvatures of the stationary points depend quite strongly on the range of the interatomic pair potential.

First, we examine the EB saddles of these two M_5 clusters. In Fig. 11 we show the probability distributions for K, $\langle K_\omega \rangle$, $\langle T \rangle$, and $\langle C \rangle$ for the $\rho=5$ M_5 cluster as it crosses this saddle; similar distributions for the $\rho=9$ M_5 cluster are given in Fig. 12. The means of the distributions for both Morse clusters are summarized in Table V, along with those for the EB saddle of LJ_5. The calculations for both Morse clusters were performed for a total energy of $E=-7.5$ ϵ.

Recall from Table IV that the EB saddle of the $\rho=9$ M_5 cluster is substantially flatter than that of the LJ_5 cluster, while the EB saddle of the $\rho=5$ M_5 cluster is more sharply pinched than the LJ_5 saddle. These differences manifest themselves in the values of $\langle K_\omega \rangle$ and K accumulated near the EB saddles of the two Morse clusters. We see from Fig. 11 and Table V that in the $\rho=5$ M_5 cluster, MD trajectory segments which cross the EB saddle experience slightly less negative curvature than trajectory segments on
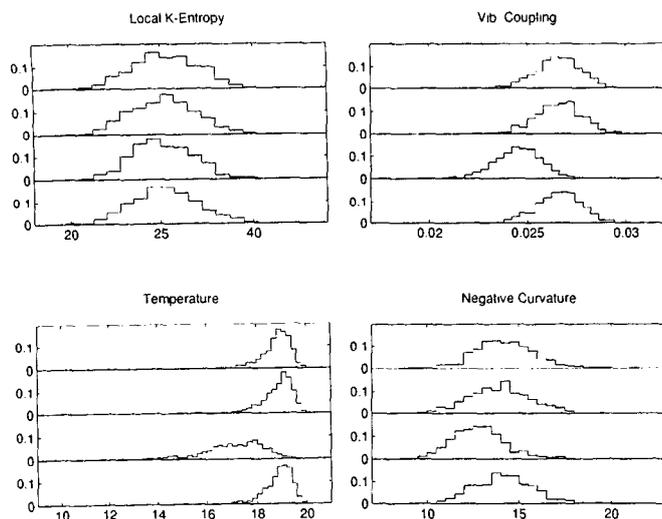
FIG. 11. Probability distributions similar to those given in Fig. 9, except for a $\rho=5$ M_5 cluster crossing its EB saddle at total energy $E=-7.5$ ϵ. The saddle-region distributions are computed from a sample of 729 EB saddle crossings, and the well-region distributions are computed from a sample of 616 trajectory segments in the potential well. Units for the abcissas are as in Fig. 2.

FIG. 13. Probability distributions similar to those given in Fig. 11, except for the DSD saddle of $\rho=5$ M_5. The saddle-region distributions are computed from a sample of 674 DSD saddle crossings, and the well-region distributions are computed from a sample of 616 trajectory segments in the potential well. Units for the abcissas are as in Fig. 2.

any other portion of the potential surface. However, the difference between the mean negative curvature in the well and saddle regions is less pronounced for this cluster than for the LJ$_5$ cluster. Furthermore, there is no apparent collimation of nearby MD trajectories near this saddle, as K has virtually the same average value in the saddle and well regions of this cluster.

In the $\rho=9$ M_5 cluster, however, the EB saddle once again is able to channel together neighboring phase space trajectories; Fig. 12 shows that K and $\langle K_\omega \rangle$ decrease sub-
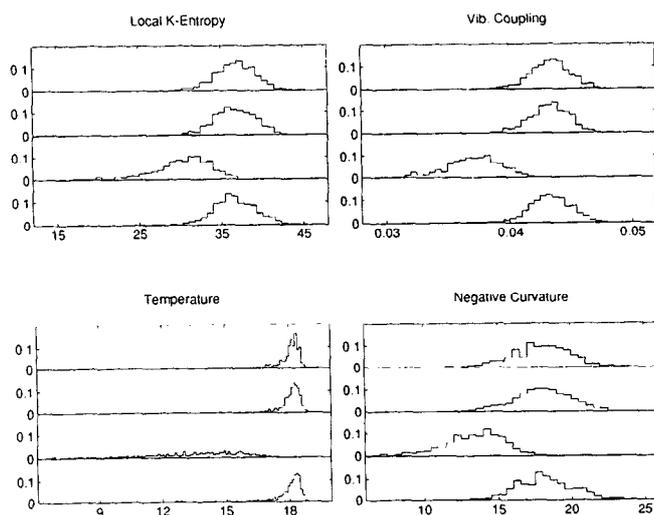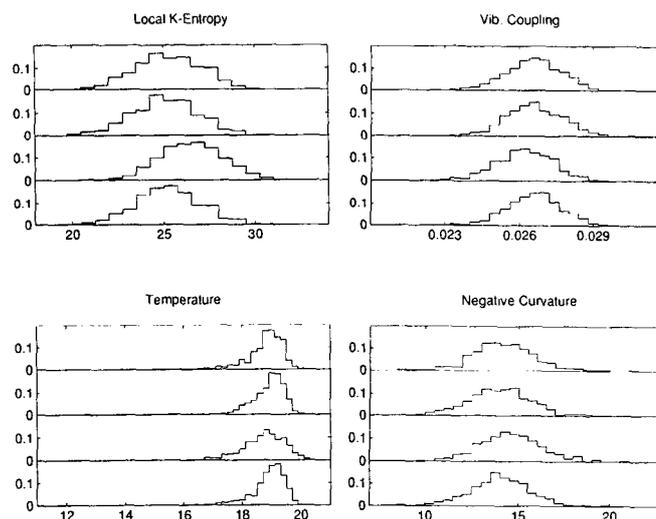

FIG. 12. Probability distributions similar to those given in Fig. 9, except for a $\rho=9$ M_5 cluster crossing its EB saddle at total energy $E=-7.5$ ϵ. The saddle-region distributions are computed from a sample of 584 EB saddle crossings, and the well-region distributions are computed from a sample of 671 trajectory segments in the potential well. Units for the abcissas are as in Fig. 2.

stantially near the EB saddle of this cluster. Thus these five-atom Morse clusters continue to follow the pattern established previously, in which flat saddles are more effective at collimating the flow of phase space trajectories and reducing the local K entropy accumulated by a cluster.

Next, we examine the behavior of $\langle C \rangle$ and $\langle T \rangle$ in these two clusters. We find that in both the $\rho=5$ and $\rho=9$ M_5 clusters, $\langle C \rangle$ and $\langle T \rangle$ decrease somewhat near the EB saddle. The decreases in these quantities are larger for the $\rho=9$ cluster, with its flatter EB saddle; however, for both M_5 clusters the decreases in $\langle C \rangle$ and $\langle T \rangle$ are statistically significant according to Student's t test and the Kolmogorov–Smirnov test. The fact that $\langle T \rangle$ decreases near the EB saddle of the $\rho=5$ M_5 cluster, while the local K entropy K does not, provides further evidence that the local K entropy accumulated by a cluster in a region of configuration space does not necessarily rise and fall in tandem with the cluster's kinetic energy there. Furthermore, the decrease in $\langle C \rangle$ near the EB saddle of the $\rho=5$ cluster suggests that in this cluster, $\langle C \rangle$ is no longer a good measure of the dynamical processes controlling the evolution of chaos near saddle points. This may be another manifestation of a "dynamical size effect" in the relatively large five-atom clusters.

Next, we turn to the DSD saddles of the two Morse clusters. Figure 13 shows the probability distributions for K, $\langle K_\omega \rangle$, $\langle T \rangle$, and $\langle C \rangle$ for the $\rho=5$ M_5 cluster as it crosses this saddle; similar distributions for the $\rho=9$ M_5 cluster are given in Fig. 14. The means of the distributions for both Morse clusters are summarized in Table VI, along with those for the DSD saddle of LJ$_5$. The calculations for both Morse clusters were again done at a total energy of $E=-7.5$ ϵ.

These results show that the DSD saddles of the two M_5 clusters have *opposite* effects on the local chaotic dynamics

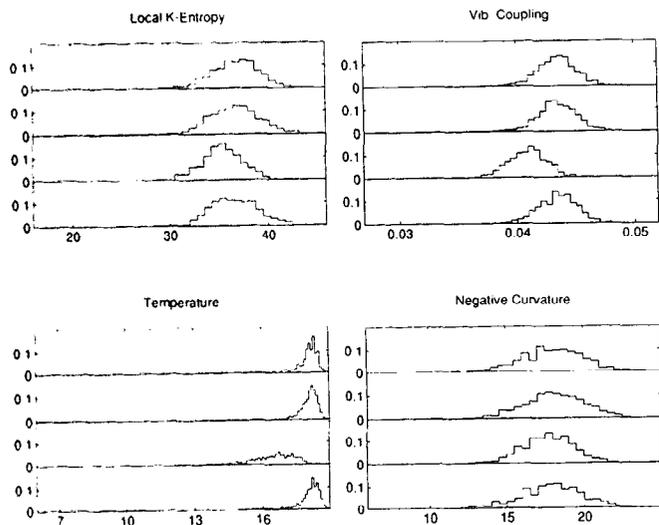Local K-Entropy

Vib Coupling

Temperature

Negative Curvature

FIG. 14. Probability distributions similar to those given in Fig. 12, except for the DSD saddle of $\rho=9$ M_5. The saddle-region distributions are computed from a sample of 727 DSD saddle crossings, and the well-region distributions are computed from a sample of 671 trajectory segments in the potential well. Units for the abcissas are as in Fig. 2.

DSD pathway

EB pathway

FIG. 15. Normal mode vibrational frequencies (in cm^{-1}) along the steepest-descent reaction paths for the DSD and EB reaction paths of a $\rho=5$ M_5 cluster. The x axis measures progress away from the saddle point in terms of a reaction path's arc length s; units are $amu^{1/2}$ Å. Only positive s values are depicted here; the reaction paths are symmetric about $s=0$. We only show that portion of the reaction path which has one imaginary frequency; this frequency, which is associated with the isomerization coordinate, is marked with a dashed line. The full reaction paths extend to $s=\pm 10.59$ $amu^{1/2}$ Å for the DSD saddle and $s=\pm 17.12$ $amu^{1/2}$ Å for the EB saddle.

of the clusters. The DSD saddle of the $\rho=9$ cluster, although it is much sharper than the EB saddle of this cluster, still acts to collimate the flow of MD trajectories slightly and thereby reduces K in the saddle region. (However, the collimating effect of this saddle is weaker than that of the same cluster's EB saddle, as we might expect from the fact that the DSD saddle is substantially more pinched.) By comparison, in the $\rho=5$ cluster, the mean negative curvature $\langle K_\omega \rangle$ and the local K entropy K actually *increase* slightly near the DSD saddle point. In fact, the $\rho=5$ cluster is locally more chaotic near the DSD saddle than in any other region of configuration space. It appears that this saddle is so sharply pinched (with $\omega_{sad} = 39.44i$ cm^{-1}) that the negative curvature of the potential surface near the saddle acts to *accelerate* the divergence of nearby phase space trajectories and thereby increases the cluster's local K entropy.

There is one peculiar point concerning the behavior of the two M_5 clusters. The DSD saddle of the $\rho=9$ cluster, which has $\omega_{sad} = 30.31i$ cm^{-1}, retains some ability to collimate nearby trajectories, but the EB saddle of the $\rho=5$ cluster, which with $\omega_{sad} = 20.99i$ cm^{-1} is substantially flatter, does not appear to collimate MD trajectories to any significant extent. Hence if we simply ranked the saddles of the two M_5 clusters in order of increasing negative curvature and in order of increasing collimating ability, these orderings would disagree with one another.

We have calculated the full DSD and EB isomerization reaction pathways for both M_5 clusters in order to gain a better understanding of the geometries of the various saddle regions in these clusters and resolve this apparent discrepancy. (Following Fukui, Kato, and Fujimoto,[39] we define the reaction path as the steepest descent path in mass-weighted Cartesian coordinates from a saddle point to a minimum. We use the CLQA algorithm of Page, Double-
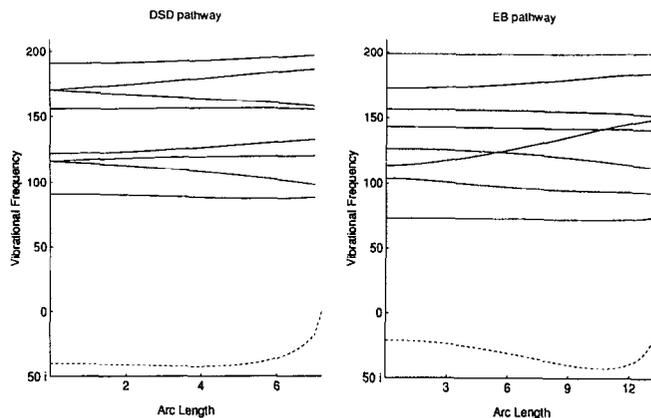
day, and McIver[40] to compute the reaction paths.) Figure 15 shows how the vibrational frequencies of the $\rho=5$ M_5 cluster vary along both the DSD and EB reaction paths of this cluster; Fig. 16 gives similar data for the $\rho=9$ cluster. The reaction paths in these clusters lie at the bottom of a nine-dimensional valley leading from the saddle point to the minimum; these figures essentially depict the local curvatures of the potential surface as a function of arc length s along the "reaction valleys" of the two clusters. We show here only those portions of the reaction paths which are
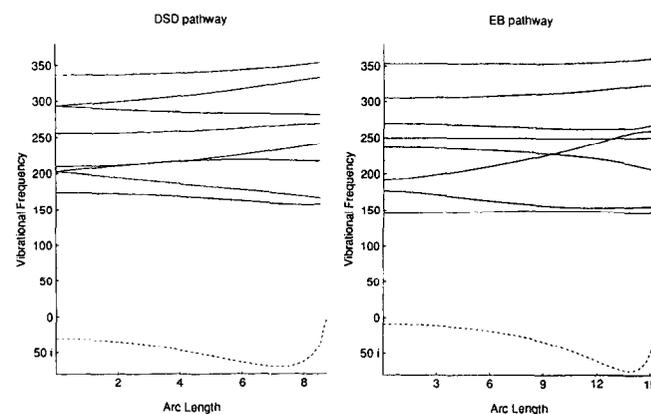
DSD pathway

EB pathway

FIG. 16. Normal mode vibrational frequencies (in cm^{-1}) along the steepest-descent reaction paths for the DSD and EB reaction paths of a $\rho=9$ M_5 cluster. The x axis measures progress away from the saddle point in terms of a reaction path's arc length s; units are $amu^{1/2}$ Å. Only positive s values are depicted here; the reaction paths are symmetric about $s=0$. We only show that portion of the reaction path which has one imaginary frequency; this frequency, which is associated with the isomerization coordinate, is marked with a dashed line. The full reaction paths extend to $s=\pm 10.75$ $amu^{1/2}$ Å for the DSD saddle and $s=\pm 17.30$ $amu^{1/2}$ Å for the EB saddle.

TABLE VII. Vibrational frequencies (in cm^{-1}) of the normal modes of $\rho=5$ and $\rho=9$ M$_5$ clusters at their respective minima and saddle points. Doubly degenerate modes are listed only once.

	Minimum			EB saddle			DSD saddle	
Species	$\rho=5$	$\rho=9$	Species	$\rho=5$	$\rho=9$	Species	$\rho=5$	$\rho=9$
E'	76.24	137.28	B_1	39.44i	30.31i	B_1	20.99i	8.64i
A_1'	113.49	208.79	B_1	90.57	173.63	A_1	73.48	145.80
E''	136.04	239.01	E	116.03	202.57	A_2	103.51	176.77
E'	140.65	252.84	A_1	122.10	209.38	B_2	113.65	192.21
A_2''	182.55	322.21	B_2	155.79	255.59	A_1	126.62	236.36
A_1'	202.04	363.49	E	170.33	293.27	B_1	142.79	249.70
			A_1	190.81	336.51	B_2	156.23	269.24
						A_1	172.69	304.92
						A_1	198.82	353.24

close enough to a saddle point to have negative curvature along the isomerization coordinate. In Table VII we give the vibrational frequencies for the two M$_5$ clusters at their respective minima and saddle points; these stationary points are the end points of the corresponding reaction paths.

We see that in both clusters, the normal mode frequencies vary fairly slowly with arc length near both the DSD and EB saddle points; hence we believe that any "rippling" of the walls of the reaction path valley is not very important in these systems. The primary difference between the reaction paths of these two clusters is simply the magnitude of the vibrational frequencies, and the magnitude of the single imaginary frequency in particular.

Figure 16 shows that in the $\rho=9$ M$_5$ cluster, the magnitude of the cluster's imaginary vibrational frequency increases substantially as the cluster moves down the reaction valley away from the saddle point. (Once the cluster begins to approach the minimum, of course, the imaginary frequency decreases sharply in magnitude.) This increase in negative curvature occurs as the reaction valley plunges sharply downward on the potential surface.

In the $\rho=5$ cluster, however, the single imaginary frequency changes less rapidly along the isomerization pathway. In fact, in the DSD reaction valley, the imaginary frequency of this cluster remains relatively constant until about $s=7$ amu$^{1/2}$ Å, after which it gradually decreases in magnitude. In the EB reaction valley, the imaginary frequency does increase in magnitude somewhat as the cluster moves away from the saddle point, but this increase is smaller than that seen in either reaction valley of the $\rho=9$ cluster. This suggests that it is important to examine the flatness of a saddle not only in absolute terms, but also in comparison to the negative curvature of the potential surface away from the saddle point. Hence although the DSD saddle of the $\rho=9$ cluster is sharply pinched in absolute terms, with $\omega_{sad}=30.31i$ cm^{-1}, the saddle region of this cluster is still significantly flatter than other portions of the potential surface, and so the cluster becomes temporarily less chaotic near the saddle point.

Finally, we note that the real frequencies of the $\rho=9$ cluster are much larger than those of the $\rho=5$ cluster, indicating that the reaction valleys of the $\rho=9$ cluster are

significantly narrower. This may enhance the decoupling effect of the $\rho=9$ saddles, because, as Eq. (1) shows, the coupling between two modes decreases sharply as the modes diverge in frequency. It is unclear whether the magnitudes of a cluster's real frequencies affect the collimating ability of a saddle. Intuitively it seems that, all other things being equal, a narrow reaction valley would collimate phase space trajectories more strongly than a wide valley. However, Wales and Berry[27] have shown that in regions of configuration space where there is at least one imaginary vibrational frequency, the magnitude of this frequency dominates the behavior of the local K entropy.

F. LJ$_6$ clusters

Next, we discuss the LJ$_6$ cluster; this is the smallest LJ cluster with two kinds of potential energy minima. The global minimum corresponds to an octahedral arrangement of the atoms, with energy $E=-12.712\ \epsilon$. There is a higher minimum in which five atoms form a trigonal bipyramid, which is capped on one face by the sixth atom; this minimum has energy $E=-12.303\ \epsilon$. The LJ$_6$ potential surface also contains two distinct kinds of first-rank saddles. One saddle, at energy $E=-12.079\ \epsilon$, joins an octahedral minimum to a capped trigonal bipyramid (CTBP) minimum; a higher saddle at $E=-11.630\ \epsilon$ joins two permutationally distinct CTBP structures. A more complete discussion of the connectivity of these saddles and minima has been presented elsewhere.[41] Because of the complexity of this surface, we have found it necessary to reduce our quench interval to 250 time steps to assemble a large ensemble of trajectory segments which cross exactly one saddle; hence the quantities we considered for the smaller clusters, such as $K^W_{3\times500}$ and $K^0_{3\times500}$, become $K^W_{3\times250}$ and $K^0_{3\times250}$ in the context of LJ$_6$.

We consider first the lower saddle, which connects two nondegenerate minima. In Fig. 17 we show several probability distributions for the quantities K, $\langle K_\omega\rangle$, $\langle T\rangle$, and $\langle C\rangle$, all calculated at $E=-10.4\ \epsilon$. Note that each portion of this figure contains *five* distributions. The topmost distribution corresponds to 750-step trajectory segments residing in the high-energy CTBP minimum, and the bottom distribution corresponds to segments residing in the octa-
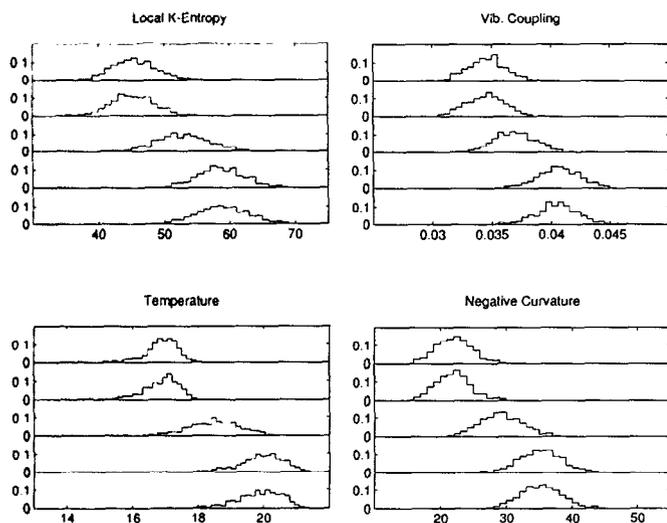
FIG. 17. Probability distributions similar to those given in Fig. 2, except for a LJ_6 cluster at total energy $E = -10.4\ \epsilon$. The saddle-region distributions are computed from a sample of 739 crossings of the lower LJ_6 saddle, and the distributions for the upper (CTBP) and lower (octahedron) minima are computed from samples of 593 and 633 trajectory segments, respectively. Units for the abcissas are as in Fig. 2. Note that the trajectory segments summarized here are each 750 steps long.

hedral minimum. The three middle distributions give, from top to bottom, results for 750-step segments immediately preceding a saddle crossing, those which include a saddle crossing, and those immediately following a saddle crossing. Only saddle crossings from the upper minimum to the lower minimum are shown here, so that each set of five distributions can be read continuously from top to bottom as representing trajectories moving from the upper well to the lower well. Saddle crossings in the reverse direction give rise to sets of distributions in which the distributions preceding and following the saddle are interchanged, but which contain statistically identical results; this shows that the direction in which the saddle is traversed is irrelevant, as we found for smaller clusters. Calculations at $E = -11.0$ ϵ produce similar results.

We see that the high-energy minimum of LJ_6 is substantially colder and less chaotic than the low-energy minimum; the high-energy well also has lower values of $\langle C \rangle$ and $\langle K_\omega \rangle$ on average. The saddle region has values of K, $\langle K_\omega \rangle$, $\langle T \rangle$, and $\langle C \rangle$ which are intermediate between those of the two minima, whereas the segments preceding or following a saddle crossing are statistically indistinguishable from those segments in the corresponding well.

It seems reasonable that the local K entropy and magnitude of negative curvature should be higher in the low-energy well than in the high-energy well. Our calculations are performed at constant total energy; hence the potential energy difference between a well's minimum and the highest energetically accessible regions in that well is larger for the lower well. If we make the plausible assumption that the degree of mode coupling and negative curvature accumulated in a well increase as we move up the sides of the well, it follows that we expect K and $\langle K_\omega \rangle$ will be highest when the cluster is in the low-energy well. It would be

interesting to compute K and $\langle K_\omega \rangle$ as functions of energy for trajectory segments in a given well, thereby probing the incremental changes in these two quantities in the energy range from E to $E + \Delta E$; this could give us some useful information about a well's shape at high energies.

Figure 17 seems to indicate that the dynamics of LJ_6 in the saddle region are intermediate between the cluster's dynamics in the two minima connected by the saddle. However, this may be an unjustified conclusion. It could be that this saddle is so sharply curved ($\omega_{\text{sad}} = 49.18i\ \text{cm}^{-1}$) that trajectories crossing the saddle do not spend a significant length of time "on the saddle," as we discussed above in the LJ_5 subsection; instead, the saddle point may simply divide each saddle-crossing segment into two parts, one in each potential minimum, with the dynamics of each subsegment being characteristic of the underlying minimum. Under this interpretation, which is essentially the same as interpretation (2) in Sec. III D, the dynamics observed for any given saddle-crossing segment would be intermediate between the dynamics in the two minima simply because each saddle-crossing segment spans both minima.

The data we present here cannot determine unambiguously which of these interpretations is correct. However, we note that the mean vibrational temperature of the saddle-crossing segments is intermediate between the mean temperatures in the two wells. We intuitively expect that the temperature in the saddle region should be lower than that in either well, because the saddle region has the highest potential energy. Hence it seems unlikely to us that at $E = -10.4\ \epsilon$ the 750-step trajectory segments crossing the CTBP→octahedron saddle of LJ_6 spend a large enough fraction of their time "on the saddle" to exhibit dynamical properties characteristic of the saddle region. Even if we consider the individual 250-step segments from which the larger 750-step segments are assembled, we find that the temperature in the saddle region is intermediate between the temperatures observed in the two wells. This suggests that for this saddle, any true saddle-region dynamics take place on a time scale shorter than 250 time steps, or 2.5 ps of real time.

Next, we discuss very briefly the high-energy saddle point, which connects two degenerate CTBP minima and is somewhat flatter ($\omega_{\text{sad}} = 34.96i\ \text{cm}^{-1}$) than the low-energy saddle point. It appears that this reduction in curvature is sufficient to allow the cluster to remain on the saddle long enough to exhibit dynamical properties representative of the saddle region, as we observe significant differences at $E = -10.4\ \epsilon$ between the 750-step well-region and saddle-region trajectory segments for this saddle. Although we do not show probability distributions for these trajectory segments here, we find that the high-energy saddle of LJ_6 is like the DSD saddle of $\rho = 5\ M_5$ in that the local K entropy of LJ_6 is actually higher in the saddle region than anywhere else on the $E = -10.4\ \epsilon$ hypersurface.

G. LJ_7 clusters

The largest cluster we consider in this paper is LJ_7; this cluster has four energetically distinct minima, which we will call "1" through "4" in order of increasing energy,

TABLE VIII. Comparison of the means of the probability distributions for K, $\langle K_\omega \rangle$, $\langle T \rangle$, and $\langle C \rangle$ for the $4 \to 2$ and $3 \to 2$ isomerization processes of LJ$_7$ at $E = -13.5\epsilon$ (see text for details). The number of trajectory segments in each sample is given by N_{UW}, N_{sad}, and N_{LW}.

Quantity	$4 \to 2$	$3 \to 2$
$K_{3\times 250}^{\mathrm{UW}}$	49.97	51.18
$K_{3\times 250}^{-3}$	49.94	50.98
$K_{3\times 250}^{0}$	57.46	57.49
$K_{3\times 250}^{+3}$	61.31	61.38
$K_{3\times 250}^{\mathrm{LW}}$	61.38	61.38
$\langle K_\omega \rangle_{3\times 250}^{\mathrm{UW}}$	20.93	22.35
$\langle K_\omega \rangle_{3\times 250}^{-3}$	21.04	22.61
$\langle K_\omega \rangle_{3\times 250}^{0}$	27.48	28.12
$\langle K_\omega \rangle_{3\times 250}^{+3}$	31.36	31.21
$\langle K_\omega \rangle_{3\times 250}^{\mathrm{LW}}$	31.55	31.55
$\langle T \rangle_{3\times 250}^{\mathrm{UW}}$	14.73	15.13
$\langle T \rangle_{3\times 250}^{-3}$	14.72	15.13
$\langle T \rangle_{3\times 250}^{0}$	15.92	16.17
$\langle T \rangle_{3\times 250}^{+3}$	17.20	17.22
$\langle T \rangle_{3\times 250}^{\mathrm{LW}}$	17.14	17.14
$\langle C \rangle_{3\times 250}^{\mathrm{UW}}$	0.0336	0.0345
$\langle C \rangle_{3\times 250}^{-3}$	0.0336	0.0345
$\langle C \rangle_{3\times 250}^{0}$	0.0354	0.0357
$\langle C \rangle_{3\times 250}^{+3}$	0.0383	0.0383
$\langle C \rangle_{3\times 250}^{\mathrm{LW}}$	0.0382	0.0382
N_{UW}	636	519
N_{sad}	655	516
N_{LW}	607	607

FIG. 18. Variation of $K_{3\times 500}^{n}$ with n for LJ$_4$ at $E = -4.2\ \epsilon$. The dashed line gives the mean value of $K_{3\times 500}^{W}$ at the same energy. Error bars extend one standard deviation in each direction.

and at least ten energetically distinct low-lying first-rank saddle points. (For a complete discussion of the LJ$_7$ potential surface, including the energies of these stationary points, we refer the reader to Refs. 21 and 32.) This cluster is of particular interest because it is the smallest Lennard-Jones cluster which exhibits distinct solidlike and liquid-like behavior over a range of temperatures.[21] In an earlier study of the evolution of chaos in LJ$_7$, we found that the K entropy of this cluster rose smoothly and monotonically with energy, showing no kinks in the "phase coexistence" range.[23]

We have studied here only two of the ten saddles of LJ$_7$: those involved in the $3 \to 2$ and $4 \to 2$ isomerization processes. We find that these two saddles, which have respective negative curvatures of $\omega_{\mathrm{sad}} = 48.88i$ cm^{-1} and $49.06i$ cm^{-1}, have properties largely similar to those of the CTBP $\to$ octahedron saddle of LJ$_6$ discussed above. In particular, we find that for both of these saddles, the saddle region has dynamical properties intermediate between those of the upper well (where K and $\langle K_\omega \rangle$ are the smallest) and the lower well (where K and $\langle K_\omega \rangle$ are the largest). We do not show the complete set of probability distributions for either of these LJ$_7$ saddles, as they appear qualitatively similar to the LJ$_6$ distributions shown in Fig. 17. Instead, we give the means of the distributions in Table VIII. (Note that we use a quench interval of 250 time steps for these computations, as we did for LJ$_6$. If we examine the individual 250-step trajectory segments obtained for LJ$_7$, we uncover the same pattern of behavior; this indi-
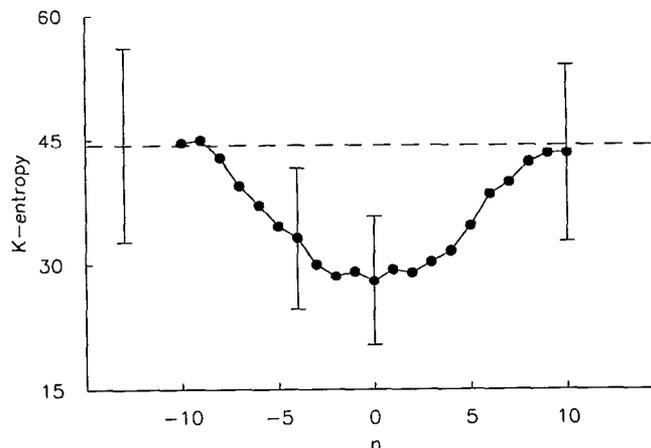
cates that any genuine saddle-region dynamics for these saddles occur on a time scale shorter than 2.5 ps.)

IV. CROSS-ENERGY AND CROSS-CLUSTER COMPARISONS

One obstacle to using the histograms presented above to make quantitative comparisons of the regularizing ability of different saddles is the fact that the saddle-crossing segments generated above may actually incorporate dynamics representative of both the saddle and well regions of the potential surface. For example, Fig. 3 showed that at $E = -1.85\ \epsilon$, a typical LJ$_3$ isomerization is complete within about 1000 time steps, or about two-thirds the duration of our 1500-step trajectory segments. Hence to fully understand the apparent convergence of well-region and saddle-region dynamics as a saddle becomes more sharply curved, we must first isolate the saddle-region dynamics. We alluded to this point above in Sec. III D, where we discussed two alternative scenarios which might explain the observed convergence of well-region and saddle-region dynamics.

The simplest way to isolate the saddle-region dynamics is to reduce the duration of our MD trajectory segments. We do this by reducing the MD time step we use by a factor of 10, to $\Delta t = 10^{-15}$ s. (We could just as easily reduce the quench interval L to generate shorter trajectory segments; however, the width of the histograms presented above increases rapidly as L is reduced, so that if L gets too small we might obscure subtle differences between sample sets.) With the reduced time step, we again search for saddle crossings and examine the behavior of $K_{3\times 500}^{n}$ as the index n moves away from $n = 0$. This gives an indication of how quickly the special nature of the saddle region dies away as a trajectory enters the deep well. For example, Fig. 18 shows how $K_{3\times 500}^{n}$ varies with n for the LJ$_4$ cluster at $E = -4.2\ \epsilon$. The dashed line gives the mean value of $K_{3\times 500}^{W}$ at this energy. We see that the influence of the saddle extends roughly over the range $-8 \leqslant n \leqslant 8$, which represents about 9 ps.
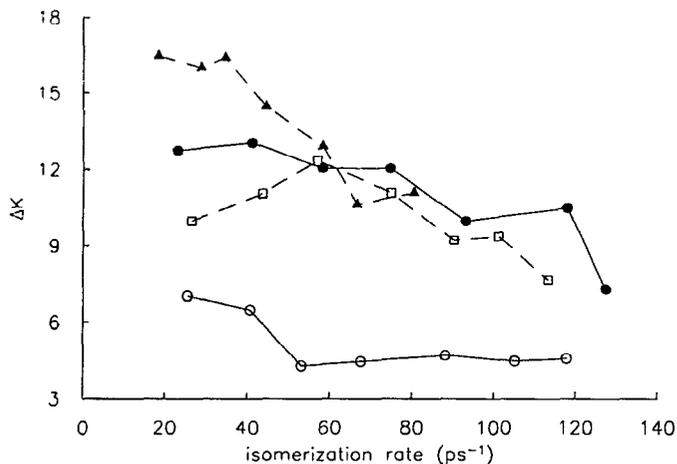
FIG. 19. ΔK for LJ_3 (open squares, dashed line), $\rho=3$ (open circles, solid line) and $\rho=6$ (solid circles, solid line) M_3, and LJ_4 (solid triangles, dashed line) clusters, plotted as a function of isomerization rate.
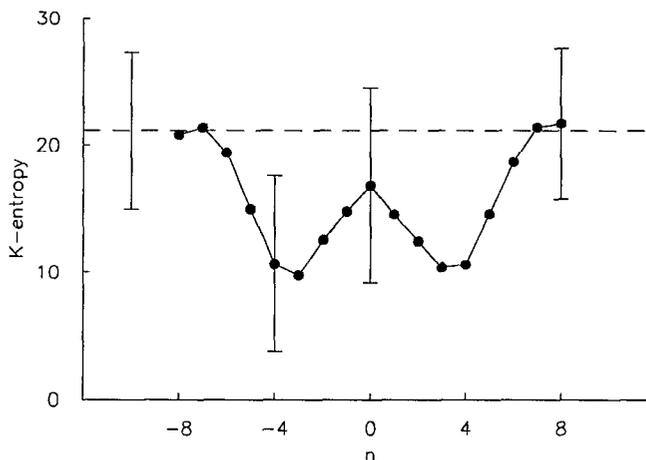
FIG. 20. Variation of $K_{3\times500}^n$ with n for $\rho=3$ M_3 at $E=-1.6$ ϵ. The dashed line gives the mean value of $K_{3\times500}^W$ at the same energy. Error bars extend one standard deviation in each direction.

Provided that $K_{3\times500}^n$ is significantly different from $K_{3\times500}^W$ for $-4\leqslant n\leqslant 4$, we can use the difference $\Delta K=K_{3\times500}^W-K_{3\times500}^0$ as a quantitative estimate of a saddle's ability to temporarily induce more regular dynamics in a cluster. This proviso ensures that the segment centered on the saddle contains only saddle-region dynamics.

We have calculated ΔK in this fashion over a range of energies for the three- and four-atom clusters studied above. For the LJ_3 and M_3 clusters, we have computed ΔK at seven equally spaced energies between -1.8 ϵ and -1.2 ϵ; for LJ_4 we have used seven equally spaced energies between -4.4 ϵ and -3.8 ϵ. Our results for all four clusters are given in Fig. 19, where we plot ΔK against the rate of isomerization across each saddle in order to correct at least partially for differences in the potential energies of the saddles. The isomerization rates given here are computed from the slope of the hazard plot[42] of consecutive well residence times in long MD trajectories.

This figure illustrates that the saddle of the $\rho=3$ M_3 cluster, which is the most sharply curved of the four saddles considered here, is clearly less effective at inducing regular dynamics than are the other three saddles. This finding coincides with the results presented in Sec. III, where we observed substantial differences between well-region and saddle-region dynamics for the LJ_3, LJ_4, and $\rho=6$ M_3 clusters, but found only small diferences between the well and saddle dynamics for the M_3 cluster with $\rho=3$. We also note that Fig. 19 confirms that the results presented in Sec. III are in fact representative of a wide range of energies for these clusters, and are not flukes or artifacts of the particular energies chosen earlier.

It appears from Fig. 19 that at low energies, the LJ_4 saddle is the most effective of the four saddles considered here in temporarily reducing a cluster's local K entropy. However, the calculations summarized here also reveal that the influence of the saddle region dies off more quickly in LJ_4 than in either LJ_3 or $\rho=6$ M_3: as we saw from Fig. 18, the influence of the LJ_4 saddle extends outward to

roughly $n=8$, while for the LJ_3 and $\rho=6$ M_3 clusters the region of reduced local K entropy typically extends to $n=12$ or 13. The competition between these two effects is responsible for the shapes of the histograms presented above. Because the fixed-length saddle-crossing segments analyzed in Sec. III contain a larger fraction of well-region dynamics for LJ_4 than for LJ_3 or $\rho=6$ M_3, the differences between the means of the well and saddle K distributions of these three clusters are comparable in magnitude despite the LJ_4 saddle's greater intrinsic ability to induce regular dynamics. If this kind of analysis were extended to the five-atom clusters studied above, it could shed some light on the question raised in Sec. III D concerning the mechanism which drives the observed convergence of well-region and saddle-region dynamics in systems with sharp saddles. The primary obstacle to this course of action is finding a time step Δt which is suitable for all of the saddles we would like to examine.

Finally, Fig. 20 illustrates an unusual feature of the $\rho=3$ M_3 saddle which was uncovered during these calculations. This figure shows that the portion of the potential surface which is most effective at reducing the local K entropy of this cluster is not the region closest to the saddle point, as we might naively expect, but is in fact somewhat removed from the saddle. Although we only give data for one energy here, we obtain similar results at each of the seven energies we have studied. We do not yet understand the reason for this behavior.

V. DISCUSSION AND CONCLUSIONS

It is helpful to begin this section by reviewing the main results of Sec. III and identifying, where possible, common patterns of behavior in the systems we have studied. The clearest way to reveal these patterns is to examine the saddles in order of increasing curvature (or decreasing flatness), instead of grouping them by cluster size as before.

For the flattest saddles we have studied, we find that the local K entropy of a cluster drops substantially near the

saddle point; examples of this type of behavior include the LJ_3, LJ_4, and $\rho=6$ M_3 clusters. As a saddle becomes sharper, the difference observed between the well-region and saddle-region local K entropy diminishes somewhat; this may reflect either the convergence of the underlying dynamics in the two regions or the possibility that fixed-length trajectory segments include a smaller fractional contribution from the saddle region when the saddle is sharply curved. This kind of behavior is seen in the LJ_5, $\rho=3$ M_3, and both M_5 clusters.

For even sharper saddles, we find instances where the saddle-region local K entropy is somewhat higher than that observed in the potential minimum, even though the mean temperature and vibrational coupling are lower near the saddle than in the well. The DSD saddle of $\rho=5$ M_5 and the high-energy saddle of LJ_6 exhibit this type of behavior.

Finally, for the sharpest saddles we have studied, the low-energy saddle in LJ_6 and the $3\rightarrow2$ and $4\rightarrow2$ saddles in LJ_7, we find that the saddle-region dynamics are intermediate between the dynamics observed in the two wells on either side of the saddle. This suggests that for these very sharp saddles, the time spent "on the saddle" is such a small fraction of our fixed-length trajectory segments that these segments actually represent an average of the dynamics characteristic of the two potential minima and not behavior representative of the saddle region. Further evidence for this view is provided by the fact that the mean temperature observed near these saddles is intermediate between the temperatures observed in the two wells, even though the saddle point is the point with greatest potential energy on the reaction path linking the two wells.

The trends we observe in the local K entropy correlate very well with the degree of negative curvature $\langle K_\omega \rangle$ which a cluster experiences in a given region of the potential surface. In addition, the asymptotic (global) K entropy curves of three- to six-atom Lennard-Jones clusters can be explained nicely in terms of these observed trends in the local K entropy.[43] Although we have not performed an exhaustive study of all of the saddles in LJ_7, the present work also sheds light on our earlier observation that the global K entropy of LJ_7 rises monotonically with energy, with no apparent kinks or plateaus associated with motion over saddles.[23] Most of the low-lying saddles in LJ_7 are rather sharp, with $27\leqslant\omega_{sad}/i\leqslant50$ cm^{-1}. If these saddles behave similarly to the ones studied here, it is not too surprising that the global K-entropy curve lacks features associated with saddle crossings; the amount of time spent on any of the saddles during a long MD trajectory is likely to be only a small fraction of the trajectory's total length. There are two saddles in LJ_7 which have $\omega_{sad}\approx20i$ cm^{-1}, a value which is comparable to the values of ω_{sad} in the five-atom clusters we have studied. However, these clusters are at such high energies ($E=-14.597$ ϵ and -14.568 ϵ) that we do not expect them to exert much influence on the cluster's dynamics at energies of interest.

We also find that the flat saddles of LJ_3 and LJ_4 are able to induce temporary and approximate quasiperiodic behavior in a cluster by decoupling its vibrational modes; the flatter LJ_3 saddle is somewhat more effective in this

regard. This quasiperiodicity manifests itself in fairly well conserved actions associated with one or more stable vibrational modes in the saddle region. Near the sharper saddles in the five-atom clusters we have studied, we find no evidence for approximate quasiperiodicity, and the saddle region generally decouples vibrational modes only very weakly.

This leads us to the question of the "dynamical size effect" mentioned earlier. We found that $\langle C \rangle$ and K followed the same trends in most of the clusters we studied here; in the DSD saddle of $\rho=5$ M_5, however, we saw that $\langle C \rangle$ decreased slightly near the saddle point, while K increased slightly there. This observation may be the signal of a transition between behavior representative of systems with only a few degrees of freedom (DOF) and that representative of many-DOF systems. If such a transition does emerge as a cluster increases in size, we might find that in large clusters (as compared with small clusters such as LJ_3) the geometric peculiarities of any given saddle are less important in determining the evolution of the K entropy with energy, simply because the properties of single vibrational modes such as the isomerization coordinate become less important in larger systems.

The distinction between K and $\langle C \rangle$ also suggests that there may be *two* contributions that a saddle region may make towards lowering the local K entropy of a cluster. A flat saddle naturally contributes less to the divergence of neighboring trajectories because of the small negative curvature of the potential surface there; this effect is quantified by $\langle K_\omega \rangle$. Those saddles near which $\langle C \rangle$ also decreases substantially may lower K further by inducing approximately quasiperiodic motion in one or more vibrational modes of the cluster. It would be interesting to probe the relative importance of these two mechanisms; to do so would require a precise criterion for determining the degree of quasiperiodic behavior near a saddle. Our approximate mode actions I_j may be a first step in this direction; another possibility would be to compare the power spectra of saddle-region and well-region trajectory segments.

We conclude by pointing out the chemical relevance of this work. Dumont and Jain[44] have recently shown that the near-separability of the vibrational Hamiltonian of LJ_3 near the saddle point, and the consequent decrease in the local K entropy there, are responsible for nonstatistical behavior in the isomerization kinetics of this cluster. The LJ_4 and M_3 clusters we have studied here may exhibit broadly similar behavior; presumably the $\rho=3$ M_3 cluster, which among our three-atom clusters has the least separable Hamiltonian in the saddle region, should also show the least degree of nonstatistical behavior.

One drawback to this line of inquiry is that it may not be feasible to study experimentally the isomerization kinetics of LJ_3-like clusters such as Ar_3, because simple infrared spectroscopic techniques are of limited utility in studying rare gas clusters. It may also be difficult to determine when Ar_3 has crossed over a saddle, as the two minima of this cluster should have identical properties. We are presently extending the current work to heterogeneous van der

Waals clusters such as $HgAr_2$ which may be more amenable to experimental analysis.

In addition, recent work of Morais and Varandas[45] suggests that the Na_3 cluster, like the weakly bound LJ_3 and M_3 clusters we have studied, becomes temporarily more regular as it passes over saddle points. The model Na_3 cluster which they studied has two nondegenerate minima and two distinct kinds of saddle points. They found that as the cluster acquires enough energy to pass over first one saddle point and then the other, the largest (global) Liapunov exponent of the cluster exhibits two sharp drops. The Na_3 cluster is an ideal candidate for experimental study, as traditional spectroscopic techniques can easily distinguish between the two distinct minima of this cluster.

ACKNOWLEDGMENTS

[1] V. I. Arnold and A. Avez, *Ergodic Problems of Classical Mechanics* (Addison-Wesley, New York, 1989).
[2] P. Brumer, Adv. Chem. Phys. **47**, 201 (1981).
[3] V. I. Oseledec, Trans. Moscow Math. Soc. **19**, 197 (1968).
[4] A. N. Kolmogorov, Dokl. Acad. SSSR **124**, 754 (1959).
[5] Y. B. Pesin, Russ. Math. Surveys **32**, 55 (1977).
[6] D. J. Wales, Nature (London) **350**, 485 (1991).
[7] M. Hénon and C. Heiles, Astron. J. **69**, 73 (1964).
[8] G. Benettin, L. Galgani, and J.-M. Strelcyn, Phys. Rev. A **14**, 2338 (1976).
[9] G. Paladin and A. Vulpiani, J. Phys. A **19**, 1881 (1986).
[10] R. Livi, A. Politi, and S. Ruffo, J. Phys. A **19**, 2033 (1986).
[11] R. Livi, A. Politi, S. Ruffo, and A. Vulpiani, J. Stat. Phys. **46**, 147 (1987).
[12] R. Livi, M. Pettini, S. Ruffo, and A. Vulpiani, J. Stat. Phys. **48**, 539 (1987).
[13] H. A. Posch and W. G. Hoover, Phys. Rev. A **38**, 473 (1988).
[14] H. A. Posch and W. G. Hoover, Phys. Rev. A **39**, 2715 (1989).
[15] H. A. Posch, W. G. Hoover, and B. L. Holian, Ber. Bunsenges. Phys. Chem. **94**, 250 (1990).
[16] D. Ruelle, Ann. Inst. Poincare **42**, 109 (1985).
[17] P. W. Cleary, J. Math. Phys. **30**, 689 (1989).
[18] C. Amitrano and R. S. Berry, Phys. Rev. Lett. **68**, 729 (1992).
[19] H. D. I. Abarbanel, R. Brown, and M. B. Kennel, J. Nonlinear Sci. **1**, 197 (1991).
[20] P. J. Robinson and K. A. Holbrook, *Unimolecular Reactions* (Wiley-Interscience, London, 1972).
[21] D. J. Wales and R. S. Berry, J. Chem. Phys. **92**, 4283 (1990).
[22] J. P. Rose and R. S. Berry, J. Chem. Phys. **96**, 517 (1992).
[23] R. J. Hinde, R. S. Berry, and D. J. Wales, J. Chem. Phys. **96**, 1376 (1992).
[24] M. Pettini, Phys. Rev. E **47**, 828 (1993).
[25] L. Verlet, Phys. Rev. **159**, 98 (1967).
[26] D. W. Heerman, *Computer Simulation Methods in Theoretical Physics*, 2nd ed. (Springer-Verlag, New York, 1990).
[27] D. J. Wales and R. S. Berry, J. Phys. B **24**, L351 (1991).
[28] H.-D. Meyer, J. Chem. Phys. **84**, 3147 (1986).
[29] W. H. Miller, N. C. Handy, and J. E. Adams, J. Chem. Phys. **72**, 99 (1980).
[30] M. Page and J. W. McIver, Jr., J. Chem. Phys. **88**, 922 (1988).
[31] R. Kosloff and S. A. Rice, J. Chem. Phys. **74**, 1947 (1981).
[32] P. A. Braier, R. S. Berry, and D. J. Wales, J. Chem. Phys. **93**, 8745 (1990).
[33] K. P. Huber and G. Herzberg, *Constants of Diatomic Molecules* (Van Nostrand–Reinhold, New York, 1979).
[34] This numbering scheme differs from the conventional system, in which v_1 denotes the symmetric stretch, v_2 the bend, and v_3 the antisymmetric stretch. Our notation is motivated by the fact that for larger clusters, different minima belong to different point groups; hence the conventional notation based on symmetry considerations is not very useful for larger, highly energized clusters which rapidly explore all of the available minima. The present system of notation avoids these difficulties and is also computationally convenient, and we adopt it for three-atom clusters as well simply for consistency.
[35] M. A. Sepúlveda, R. Badii, and E. Pollak, Phys. Rev. Lett. **66**, 1226 (1989).
[36] W. H. Press, B. P. Flannery, S. A. Teukolsky, and W. T. Vettering, *Numerical Recipes* (Cambridge University, New York, 1989), Chap. 13.
[37] W. N. Lipscomb, Science **153**, 373 (1966).
[38] B. F. G. Johnson, J. Chem. Soc. Chem. Commun. 27 (1986).
[39] K. Fukui, S. Kato, and H. Fujimoto, J. Am. Chem. Soc. **97**, 1 (1975).
[40] M. Page, C. Doubleday, and J. W. McIver, Jr., J. Chem. Phys. **93**, 5634 (1990).
[41] R. S. Berry, P. Braier, R. J. Hinde, and H.-P. Cheng, Isr. J. Chem. **30**, 39 (1990).
[42] E. Helfand, J. Chem. Phys. **69**, 1010 (1978).
[43] R. J. Hinde, Ph.D. thesis, The University of Chicago, 1992.
[44] R. S. Dumont and S. Jain, J. Chem. Phys. **97**, 1227 (1992).
[45] V. M. F. Morais and A. J. C. Varandas, J. Phys. Chem. **96**, 5704 (1992).